Key Points:

- We derived a self-consistent analytical solution for a zero-buoyancy plume model to understand the steady-state tropical atmosphere
- The plume model suggests that increased mixing enhances convective mass flux via greater cloud evaporation or reduced atmospheric stability
- Steady-state simulations with finer grids, indicating stronger mixing, show increased anvil cloud amount and upper-troposphere mass flux

Author Contributions:

Conceptualization: Zeyuan Hu, Nadir Jeevanjee, Zhiming Kuang
Formal analysis: Zeyuan Hu, Nadir Jeevanjee, Zhiming Kuang
Funding acquisition: Zhiming Kuang
Methodology: Zeyuan Hu, Nadir Jeevanjee, Zhiming Kuang
Software: Zeyuan Hu
Supervision: Nadir Jeevanjee, Zhiming Kuang
Visualization: Zeyuan Hu
Writing – original draft: Zeyuan Hu
Writing – review & editing: Zeyuan Hu, Nadir Jeevanjee, Zhiming Kuang

A Refined Zero-Buoyancy Plume Model for Large-Scale Atmospheric Profiles and Anvil Clouds in Radiative-Convective Equilibrium

Zeyuan Hu[1] , **Nadir Jeevanjee[2]** , **and Zhiming Kuang[1,3]**

[1]Department of Earth and Planetary Sciences, Harvard University, Cambridge, MA, USA, [2]Geophysical Fluid Dynamics Laboratory, Princeton, NJ, USA, [3]John A. Paulson School of Engineering and Applied Sciences, Harvard University, Cambridge, MA, USA

Abstract A simple analytical model, the zero-buoyancy plume (ZBP) model, has been proposed to understand how small-scale processes such as plume-environment mixing and evaporation affect the steady-state structure of the atmosphere. In this study, we refine the ZBP model to achieve self-consistent analytical solutions for convective mass flux, addressing the inconsistencies in previous solutions. Our refined ZBP model reveals that increasing plume-environment mixing can increase upper-troposphere mass flux through two pathways: increased cloud evaporation or reduced atmospheric stability. To validate these findings, we conducted small-domain convection-permitting Radiative-Convective Equilibrium simulations with horizontal resolutions ranging from 4 km to 125 m. As a proxy for plume-environment mixing strength, the diagnosed entrainment rate increases with finer resolution. Consistent with a previous study, we observed that both anvil cloud fraction and upper-troposphere mass flux increase with higher resolution. Analysis of the clear-sky energy balance in the simulations with two different microphysics schemes identified both pathways proposed by the ZBP model. The dominant pathway depends on the relative strengths of evaporation cooling and radiative cooling in the environment. Our work provides a refined simple framework for understanding the interaction between small-scale convective processes and large-scale atmospheric structure.

Plain Language Summary High, anvil-shaped clouds in the tropics significantly impact our climate, but simulating them accurately is challenging. Our study investigates how small-scale mixing affects anvil clouds and vertical air movement in the upper atmosphere. We refined a simple analytical model, which treats convection as a single plume, to better understand these processes. Our results show that stronger mixing increases the amount of air moving upward, either through increased cloud evaporation or reduced atmospheric stability. We confirmed these findings with km-scale numerical simulations at various grid sizes. Finer resolutions, indicating stronger mixing, led to more anvil clouds and greater upward air movement, supporting our simple plume model's predictions. These insights improve our understanding of how small-scale processes influence the large-scale atmosphere.

1. Introduction

Uncertainty associated with cloud and convection remains one of the most significant factors contributing to climate feedback uncertainties in future climate change projections (e.g., Bony et al., 2015; Sherwood et al., 2014; Zelinka et al., 2020). Representing such small-scale processes in the coarse-grid global climate models requires parameterization of convection and cloud microphysics, which have become a major source of uncertainty. In recent years, the scientific community has made significant strides in developing and examining global storm-resolving models with grid sizes of 1–5 km (e.g., Satoh et al., 2019; Stevens et al., 2019). By explicitly resolving deep convection, GSRMs do not require the use of convective parameterization, but the actual convective mixing strength can still be sensitive to horizontal and vertical resolution, sub-grid turbulence models, and advection schemes. It remains unclear how the large-scale atmosphere state in km-scale simulations can be influenced by the representation of the small-scale mixing processes.

A simple analytical model that can illustrate the effect of small-scale processes on large-scale tropical atmospheric state is the zero-buoyancy plume (ZBP) model (Romps, 2014, 2021; Singh & Neogi, 2022; Singh & O'Gorman, 2013; Singh et al., 2019). This model can analytically solve for the lapse rate and relative humidity profiles of an equilibrium atmosphere when small-scale processes like plume-environment mixing strength and

cloud evaporation rate are specified. The model makes the approximation that the ensemble of convection can be treated as a single neurally buoyant plume (Singh & O'Gorman, 2013), which is justified by the fact that the buoyancy of convective plumes is relatively small due to mixing and convective adjustment (usually less than 1 K in observations and simulations, e.g., Lawson & Cooper, 1990; Romps & Charn, 2015). The ZBP model has been used to explain many aspects of the equilibrium atmosphere, especially the balance and sensitivities of radiative-convective equilibrium (RCE) simulations. Romps (2014) shows that the tropical relative humidity can be analytically expressed as a balance between convective detrainment and environment subsidence, and is independent of surface temperature. Singh et al. (2019) introduced the large-scale vertical motion into the model and can reproduce the temperature and moisture mean state response to large-scale forcing in RCE simulations. Romps (2021) expanded the model to account for convective aggregation and can reproduce how thermal profiles respond to the degree of aggregation. Singh and Neogi (2022) coupled the ZBP model with a dynamical solver for large-scale vertical motion through weak temperature gradients. It was able to reproduce a top-heavy large-scale upward motion like the large-scale circulation pattern in tropical convection-active ascent regions which is warmer than the tropical mean. Singh and Neogi (2022) also showed that entrainment mixing helps amplify this top-heavy response. In summary, the ZBP model can be a useful framework for understanding the fundamental aspects of the large-scale atmosphere state and the influence of small-scale processes.

One caveat of the solutions of the ZBP model provided in Singh and Neogi (2022) and Romps (2021) is the solution of the convective mass flux profile. Convective mass flux is of great importance because it drives precipitation and controls cloud fraction through mass detrainment. In their solutions, Singh and Neogi (2022) and Romps (2021) assumed equal fractional entrainment rate and detrainment rate, which in principle should suggest no vertical change in the convective updraft mass flux through the mass conservation. However, their solution of mass flux profile, for example, Figure 7 in Singh and Neogi (2022), does not follow this assumption, especially in the upper troposphere where mass flux rapidly decreases. Singh and Neogi (2022) acknowledged this caveat as an approximation for simplicity and examined at which heights this approximation in their solutions is reasonable.

In km-scale convection-permitting equilibrium simulations, it remains unclear how small-scale mixing can influence convective mass flux and cloud fraction. At shorter time scales, mixing can influence individual convective updraft through entrainment and detrainment. At longer time scales, time-averaged mass flux is required to provide enough latent heating to balance the atmospheric radiative cooling through condensation. The processes involved in this energy balance can be influenced by the small-scale mixing through changing thermal structure and evaporation efficiency. In km-scale or hm-scale convection-permitting simulations, although there are no direct parameters like entrainment rate that control convective mixing, some model parameters, for example, model resolution, could potentially change mixing strength. In idealized squall line simulations, Bryan et al. (2003) showed decreasing grid size from the order of 1 km to the order of 100 m tends to give more turbulent flow with resolved entrainment and overturning within clouds. By perturbing horizontal resolution in small-domain RCE simulations, Jeevanjee and Zhou (2022) (hereafter, JZ22) showed a striking dependence of anvil cloud fraction and mass flux on horizontal resolution. In their simulations with finer resolution, they observed that the updraft mass flux and anvil cloud fraction rise dramatically, with peak anvil cloud fraction from approximately 5% at the coarsest 16 km grid size to over 40% at the finest 62.5 m resolution. They argued that finer horizontal resolution corresponds to stronger mixing which can enhance cloud evaporation and lower precipitation efficiency. A smaller precipitation efficiency would then lead to greater cloud-base mass flux, which would lead to more mass flux reaching the upper troposphere and producing more anvil clouds. However, given the unconstrained effects of entrainment and detrainment, Jeevanjee (2022) showed that the relation between cloud base mass flux and precipitation efficiency is not necessarily tightly constrained; furthermore, and it is unclear whether changes in cloud base mass flux can consistently project to the upper troposphere.

In this work, we study and illustrate how small-scale mixing can influence the mass flux and anvil cloud fraction. We first refine the ZBP model to get self-consistent solutions of mass flux profiles. We show that the inconsistency in previous studies comes from the ill-posed equations due to the mismatch in the numbers of equations and unknown variables. We provide a well-posed solution by adjusting unknown variables and incorporating a boundary condition involving RCE. In this refined ZBP model, we find that increasing mixing strength can lead to an increase of upper troposphere mass flux through two pathways, either more cloud evaporation or weaker stability in the upper troposphere. Furthermore, following JZ22, we test the dependence of mass flux and cloud fraction on mixing strength in small-domain RCE simulations by changing the horizontal resolutions with a fixed

domain size. Consistent with JZ22, we found anvil cloud fraction and upper troposphere mass flux increase with increasing horizontal resolution. Through clear-sky energy balance analysis, our RCE simulations with two different microphysics schemes show two pathways as the ZBP model suggests. Compared to JZ22, our ZBP model and RCE simulations reveal an additional mechanism pathway in which the stability change in the upper troposphere can dominate the mass flux change. This pathway dominates when evaporative cooling is much smaller than the radiative cooling in the upper troposphere. However, it should be noted that the ZBP model primarily serves to illustrate these pathways and mechanisms, rather than directly emulate the simulation results. In addition to the sensitivity of anvil cloud fraction to resolution, we also noticed a large sensitivity of anvil cloud fraction to the microphysics scheme, which is also found in previous studies (e.g., Hu et al., 2021; Igel et al., 2015; Powell et al., 2012) and deserves further study.

The rest of the manuscript is structured as follows: in Section 2 we briefly describe the setup of the refined ZBP model with the complete derivation in Appendix A. Section 3 describes the insight from the solutions of the ZBP model. We show how large-scale equilibrium state mass flux and thermal profiles can respond to small-scale processes. Section 4 shows the results from the numerical RCE simulations. Section 5 is the discussion and summary.

2. Refined ZBP Model With a Self-Consistent Solution of Mass Flux

In this section, we describe the setup of our refined ZBP model. We briefly cover the most essential ingredients here, while the readers can find the complete derivation with a more detailed explanation in Appendix A. The ZBP model we use here is adapted from the ZBP model in Singh and Neogi (2022). The model presented in Singh and Neogi (2022) includes a thermodynamic component, that is, the ZBP model, and a dynamical solver that uses the assumption of weak-temperature gradients to solve large-scale vertical motion. In this study, we utilize only the ZBP model without the dynamical solver to examine RCE with no large-scale vertical velocity.

The ZBP model assumes that the steady state of the atmosphere can be represented by a single updraft plume and downdrafts in the environment. The updraft and environment can exchange mass, water, and heat via entrainment and detrainment. The model assumes that the steady state of the atmosphere is neutrally buoyant with respect to the entraining plume (Singh & O'Gorman, 2013), that is, the temperature in the updrafts is the same as the temperature in the environment at the same level. The virtual effect of vapor is ignored. Figure S1 in Supporting Information S1 shows that the time-averaged temperature anomaly (relative to the domain-mean) in the convective updraft in our cloud-resolving numerical simulations is indeed within 1 K except at the top of troposphere above 14 km. The model further presumes that the radiative cooling rate is a function of temperature. We choose to specify that the radiative cooling rate is $-1\,\mathrm{K\,day^{-1}}$ when the temperature is above 250 K, and decreases to 0 at 200 K through a cosine function. By combining conservation equations (for mass, water vapor, and moist static energy) and the hydrostatic balance equation, this ZBP model can be written as a system of ordinary differentiate equations (ODE):

$$\frac{\partial}{\partial z}(M_c, p, q, T) = F(M_c, p, q, T | \epsilon, \mu) \tag{1}$$

where M_c, p, q, T represent the convective mass flux, pressure, specific humidity, and temperature. ϵ and μ are the entrainment rate and the evaporation parameter, which are the model parameters that we need to specify and can adjust. Given boundary conditions (we will discuss this later), we can solve Equation 1 to get the vertical profiles of mass flux, pressure, specific humidity, and temperature.

The major difference to the solution in Singh and Neogi (2022) is the treatment of mass flux and detrainment rate. Unlike our ODE Equation 1, in Singh and Neogi (2022), the mass flux is not included in their ODE equation. They assume the detrainment rate δ equals the entrainment rate ϵ. This would imply no vertical change in the convective updraft mass flux through the mass conservation equation:

$$\frac{\partial M_c}{\partial z} = M_c(\epsilon - \delta) \tag{2}$$

However, since Singh and Neogi (2022) have more equations than unknown variables, they can still diagnose a mass flux profile by using the rest of their equations. This diagnosed mass flux profile will be inconsistent with the assumption of equal entrainment and detrainment rates. Singh and Neogi (2022) acknowledged this caveat as an approximation for simplicity. In this study, we relax this approximation and use a self-consistent method of solving the equations by allowing the difference between the fractional detrainment rate and the fractional entrainment rate to vary vertically. The shape of the mass flux profile is partially constrained by energetics, as the mass flux needs to diminish where radiative cooling starts to rapidly decrease in the upper troposphere. Therefore, the entrainment rate and detrainment rate cannot be completely independent. To specify the strength of plume-environment mixing in the model, one could specify either the entrainment rate, detrainment rate, or some other variable, such as the mixing rate in Bretherton et al. (2004). Here, for simplicity, we choose to specify the entrainment rate to impose the strength of plume-environment mixing. In this way, we have the same number of equations as the number of unknown variables.

Following Singh and Neogi (2022), in this model, cloud evaporation is parameterized as:

$$s_{\text{evap}} = \mu d(q^* - q) \tag{3}$$

where d is mass detrainment, q^* and q is the specific humidity in the saturated updraft and in the environment. A larger evaporation parameter μ tends to produce more cloud evaporation in the environment. This equation has two underlying assumptions. First, this equation assumes that the detrained flux of condensate equals $\mu_1 dq^*$, that is, proportional to the detrained flux of water vapor with a scaling factor μ_1. Second, it assumes that the fraction of detrained condensate that evaporates (as opposed to precipitating to the ground) is $\mu_2(1 - q/q^*)$, where $(1 - q/q^*)$ approximately equals $1 - \mathcal{R}$ ($\mathcal{R}$ represents relative humidity RH) and μ_2 is another scaling factor. The μ in Equation 3 is simply $\mu_1\mu_2$. It is likely that the ratio of condensate evaporation versus conversion to rain is less sensitive to RH when RH is far less than 1. We also explored a different parameterization defined by $s_{\text{evap}} = \mu dq^*(1 - \mathcal{R})^{0.5}$, which yielded results that are qualitatively similar (not shown).

Once we specify the boundary conditions, we can solve the system of ODEs. Here we specify the temperature, pressure, and specific humidity directly at the cloud base level at $z = 500$ m, but we cannot directly specify the mass flux at the cloud base. In principle, the amount of convection that can happen is determined by the amount of latent heating required to balance the radiative cooling in the whole atmosphere. That is, the mass flux at the cloud base is not determined by boundary processes but by the energy balance in the whole free troposphere. To satisfy RCE at all model levels, we require the mass flux to diminish to zero at the same level where the radiative cooling rate goes to zero (for the simple radiation we specify, this is the level where the temperature goes to 200K). We can search different cloud base mass flux values and find a unique value that satisfies this RCE condition. We can then use this cloud base mass flux value to integrate the ODE equation upward to get the full atmosphere profiles. The full details of the model equations, derivation of the solution, and some sensitivity tests are documented in Appendix A.

3. Insights From the Refined ZBP Model

With this refined ZBP model, we now test the sensitivity of the steady-state atmosphere profiles to the entrainment rate and the evaporation rate. One should focus primarily on the profile behavior below around 12–14 km, above which the neural buoyancy assumption is no longer justified. First, we test the sensitivity to the fractional entrainment rate ϵ for two different values of the evaporation parameter μ (Figure 1, upper row for $\mu = 1$ and lower row for $\mu = 0.1$). In both cases, with an increase in the entrainment rate, we observe an increase in the detrainment rate, mass flux, relative humidity, and latent cooling in the environment. The temperature in the upper troposphere is colder with a higher entrainment rate, and the dry stratification (ds/dz, where s is dry static energy) is lower. Figure 1 suggests that increasing the entrainment rate can lead to a relatively uniform increase in mass flux from cloud base to anvil level.

Considering the dry static energy balance $M_{\text{c}} = (Q_{\text{rad}} + Q_{\text{lat}})/\left(\frac{\partial s}{\partial z}\right)$, increasing entrainment rate leads to both increasing cloud evaporation and less stratified upper troposphere. Both these factors can contribute to an increasing mass flux. When cloud evaporation is efficient (Figure 1 with $\mu = 1$), the change of latent cooling can dominate the change in mass flux. However, when cloud evaporation is weak (Figure 1 with $\mu = 0.1$), the
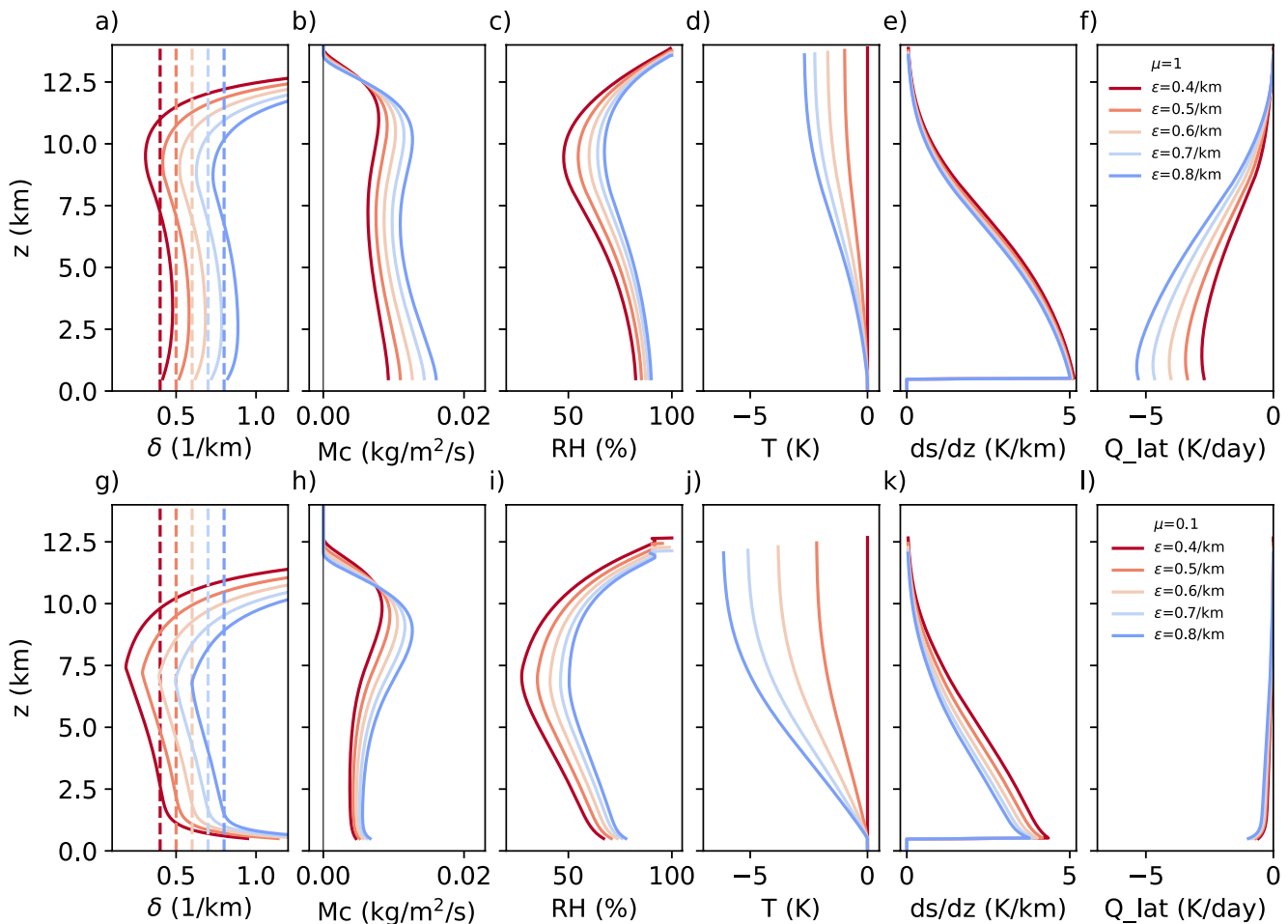
Figure 1. Atmosphere profiles in the zero-buoyancy plume model with varying entrainment rates (warmer color represents lower entrainment rate). The upper row has a cloud evaporation parameter $\mu = 1$. The variables shown are (a) detrainment rate, (b) updraft mass flux, (c) relative humidity, (d) temperature, (e) the vertical gradient of dry static energy, and (f) latent heating rate due to cloud evaporation in the environment. The dashed lines in panel (a) are the profiles of the prescribed entrainment rate. The temperature in panel (d) is shown as deviation to one of the simulations, which is denoted by the red line with zero deviation. The lower row is similar to the upper row but with cloud evaporation parameter $\mu = 0.1$.

absolute latent cooling and the change of latent cooling are small compared to the prescribed radiative cooling rate. The change in stratification due to increasing entrainment rate is larger with small μ and can dominate the change of mass flux. Environmental relative humidity is important in determining the sensitivity of stability to changing the entrainment rate. The relative humidity is lower with $\mu = 0.1$ than with $\mu = 1$ (Figures 1c and 1i). In this ZBP model, the lapse rate in the environment equals to the lapse rate of the updraft plume. The impact of the entrainment dilution on the updraft lapse rate depends on the environmental saturation deficit (Equation A16). Therefore, a small μ tends to make stability more sensitive to the change of entrainment (Figures 1e and 1k).

In Figure 2, we maintain a constant fractional entrainment rate as $0.5\ \mathrm{km}^{-1}$ and test the sensitivity of atmosphere profiles to the evaporation parameter μ. As the evaporation strength increases, the free troposphere is warmer, deeper, and more moist (Figures 2b–2d). The increased relative humidity is a direct result of the enhanced efficiency of cloud evaporation. This is consistent with JZ22 which shows that the evaporation efficiency plays an important role for the relative humidity, especially in the upper troposphere. Consequently, with a more moist atmosphere, the entrainment dilution has a weaker impact on the temperature of the updraft plume, resulting in a warmer and deeper troposphere. In the lower troposphere, we see a clear increase in mass flux with increasing cloud evaporation. However, in the upper troposphere, the mass flux adjustment is more akin to an upward shift with weak change in magnitude. The peak mass flux near the anvil level remains largely unchanged, suggesting a minor change in the convergence of mass flux at higher altitudes. From the perspective of the energy budget, an
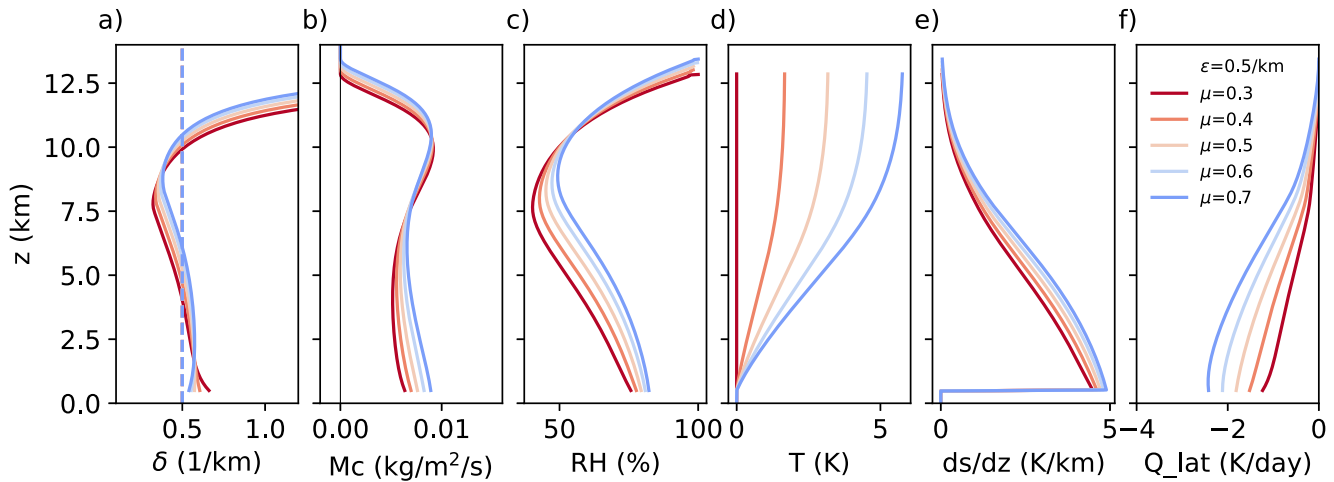
Figure 2. Similar to Figure 1 but with a fixed entrainment rate of 0.5 km^{-1} and varying cloud evaporation parameter (warmer color represents less efficient cloud evaporation).

increase in the evaporation rate could induce greater latent cooling. However, this is offset by an increase in stability in the upper troposphere, effectively suppressing the change in mass flux (Figures 2e and 2f).

In addition to the energy budget, a different way to understand the mass flux response to entrainment rate change in this analytical model is through the Betts's rule described in Jeevanjee (2022). Consider the water vapor budget for the atmosphere above a certain level z. The mass flux at z satisfies:

$$M_c q^*(1 - \mathcal{R}) = \int_z^{z_{top}} -c_p \rho Q_{rad} dz/\ell_v \tag{4}$$

where z_{top} is the top of the atmosphere, c_p is the isobaric specific heat, ρ is air density, ℓ_v is the latent heat of vapourization. The left-hand side (LHS) represents the net water vapor transported upward across level z by saturated updraft and unsaturated subsidence. In a steady state, this transport of vapor must be balanced by the net condensation, which is required to balance the total radiative cooling above level z (the right-hand side, RHS). Since in the model, the prescribed radiative cooling is constant at $-1\,\mathrm{K\,day^{-1}}$ for the troposphere where the temperature is larger than 250 K, the change in the RHS is relatively small, especially for the lower and middle troposphere. When we increase the horizontal mixing (Figure 1), the relative humidity increases, and more clouds get detrained. The temperature through the whole troposphere also decreases, leading to a decreasing saturation vapor specific humidity q^*. To satisfy the equation, the mass flux on the LHS has to increase to provide sufficient upward vapor transport.

4. Sensitivity of Small-Domain RCE Simulations on Horizontal Resolution

4.1. Experiment Setup

We use the System for Atmosphere Modeling (SAM; Khairoutdinov & Randall, 2003), version 6.10.6, configured as a cloud-resolving model. We run three-dimensional RCE simulations using the same domain size of 128 km × 128 km with different horizontal resolutions of 4 km, 2 km, 1 km, 500 m, 250 m, and 125 m. All simulations use 60 vertical levels with the model top located at 26 km and a rigid-lid top boundary condition. The vertical grid spacing increases from 75 m near the surface to a constant of 500 m throughout the whole free troposphere and above. The model time step is specified as 15 s but will automatically reduce by half iteratively when the Courant–Friedrichs–Lewy (CFL) condition is not satisfied. The effective time step for finer resolutions will be shorter than that for coarser resolutions to satisfy the CFL condition. A sponge layer is located in the upper 30% of the model domain (i.e., above 18 km). The radiation scheme used is the Rapid and Accurate Radiative Transfer Model for General Circulation Models (RRTMG) (Iacono et al., 2008). A simple Smagorinsky-type scheme (Khairoutdinov & Randall, 2003) is used for the effect of subgrid-scale motion. In this subgrid-scale

scheme, the horizontal grid size does not explicitly change the mixing length, which is set to the vertical grid size in unstable atmosphere and is modified by the local stability in stable atmosphere. When doing the horizontal scalar diffusion, the eddy diffusivity is scaled by a grid factor that depends on horizontal grid size. However, the resolution dependence shown in the later sections is largely unchanged when we turn off the horizontal scalar diffusion (not shown). We use a constant solar insolation (no diurnal cycle) with a fixed solar constant of 683.5 W m^{-2} and a zenith angle of 50.5°. The domain-averaged horizontal wind is nudged to zero at each vertical level with a nudging time scale of 1 hr. Sea surface temperature is uniformly fixed at 303 K.

For the simulations with horizontal resolution ranging from 4 km to 250 m, the first 50 days are taken as the model spinup and considered long enough for the model to reach equilibrium. After the 50-day spinup, a 20-day post-equilibrium period is used for analysis. The 30-samples-per-hour data are then averaged to obtain an hourly output of domain-mean statistics. For the 125m-resolution simulation, we initialize the simulation with the equilibrium temperature and moisture profiles from the 500m-resolution simulation. Then we run only 30 days for spinup and 5 days for analysis.

We use two different microphysics schemes: SAM single-moment scheme (SAM1MOM, Khairoutdinov & Randall, 2003) and a double-moment Morrison et al. (2005) scheme. The only prognostic water species in the SAM1MOM scheme are the total water (vapor plus non-precipitating condensate) and precipitating water. The SAM one-moment scheme uses an instantaneous saturation adjustment to determine the partition of water vapor, generate and remove cloud condensate. Cloud condensate is then divided into liquid and/or ice phases based on temperature. Between 273.16 and 253.16 K, the partitioning of cloud condensate into cloud ice and liquid water depends linearly on the temperature (at 253.16 K, all condensate is ice; at 273.16 K, all condensate is liquid water). Similarly, precipitating water is diagnostically partitioned into rain, snow, and graupel based on the temperature. The saturation adjustment occurs at each effective time step. It should be noted that with finer resolution, saturation adjustment occurs faster given the effective time step is smaller. Morrison et al. (2005) scheme includes many more pathways for conversion between different hydrometeors. Morrison et al. (2005) scheme prognostically calculates the mixing ratio and number concentration of cloud water, cloud ice, rain, snow, and graupel. Regarding cloud-radiation coupling, for frozen water species, only cloud ice is radiatively active in the SAM1MOM scheme, while both cloud ice and snow are radiatively active in the Morrison et al. (2005) scheme. In addition, different codes are used to calculate cloud optical depth for the two microphysics schemes before the radiation calculation. We tried turning off the cloud-radiative interactions for both microphysics schemes, assuming clear-sky conditions in all radiation calculations. The atmosphere mean state and resolution sensitivity for the SAM1MOM scheme remains qualitatively the same. For Morrison et al. (2005) scheme, the impact of turning off cloud-radiation interactions on the resolution dependence is discussed in a later section.

Morrison et al. (2005) scheme tends to produce more optically thin ice clouds in the upper troposphere (e.g., Hu et al., 2021; Powell et al., 2012) and consequently strong atmospheric cloud radiative heating in the middle and upper troposphere. This stronger atmospheric cloud radiative heating can stabilize the upper troposphere and weaken the convective updraft reaching the upper troposphere (Hu et al., 2021). It is unclear why the Morrison et al. (2005) scheme tends to produce excessive anvil clouds compared to other microphysics schemes including the SAM1MOM scheme. Powell et al. (2012) argued that the excessive anvil clouds are due to the large cap value for ice number concentration in the Morrison et al. (2005) scheme. However, even with a much smaller cap value in the latest version of the SAM, the Morrison et al. (2005) scheme still tends to produce more anvil clouds (e.g., Hu et al., 2021). Unlike the SAM1MOM scheme, the Morrison et al. (2005) scheme does not use saturation adjustment for cloud ice (but has saturation adjustment for liquid cloud), potentially leading to slower ice sublimation. In addition to sublimation, the Morrison et al. (2005) scheme also seems to have slower cloud ice sedimentation (see later in Figure 5) compared with the SAM1MOM scheme. Other microphysical processes that convert ice clouds to snow are also important sinks of cloud ice (Figure 8 in Bao et al. (2019)). It is worth studying in the future to understand which of these microphysical processes are responsible for the excessive anvil clouds in the Morrison et al. (2005) simulations.

4.2. Impacts of Horizontal Resolution on Mean Atmospheric State

To confirm that changing horizontal resolution is indeed an effective way of changing mixing strength, we first examined how the entrainment rate varies across different simulations. Here, we choose to illustrate the entrainment change with a method of a spectrum of entraining plumes, following Kuang and Bretherton (2006). In

this plume spectrum calculation, we use environmental profiles from each simulation to infer the entrainment rate for updrafts. We take the Morrison et al. (2005) simulations for illustration, while the SAM1MOM simulations have very similar results (not shown). In Figures 3a and 3c, we show the convective updraft mass flux distribution in the space of frozen moist static energy (FMSE) and height. FMSE is defined as $c_p T + gz + L_v q - L_f q_i$. The individual lines represent the FMSE profiles of entraining plumes rising from the cloud base at different entrainment rates. Here, these entraining plumes are assumed to follow $dh/dz = -\epsilon(h - h_{env})$, where h_{env} is the time-mean, domain-mean FMSE profile and ϵ is the fractional entrainment rate. The convective updrafts in the 125 m-resolution simulation (Figure 3c) shift toward FMSE profiles with higher entrainment rate compared to the updrafts in the 4 km-resolution simulation (Figure 3a). Once we have computed the FMSE profiles with varying entrainment rates, we can measure the amount of mass flux allocated to each entrainment rate bin. Subsequently, we can represent the updraft mass flux in the space of height and entrainment rate. As shown in Figures 3b and 3d, it is apparent that the mass flux distribution shifts toward higher entrainment rates with finer resolution. There is also a shift toward lower entrainment rates with higher altitudes, with roughly a factor of 3 difference in mode entrainment rate between lower tropospheric and upper tropospheric plumes (Kuang and Bretherton (2006), see also Zhou and Xie (2019)). It is important to note that the sensitivity of the entrainment rate on grid size could be model-dependent. In the SAM model, the entrainment mixing seems to be contributed mainly by numerical diffusion, while sub-grid diffusion is very weak in the free troposphere. Whether the resolution dependence of the entrainment rate would hold with other models using different advection and sub-grid diffusion schemes needs to be further tested.

In our small-domain RCE simulations, increasing horizontal resolution leads to increased relative humidity and convective updraft mass flux (Figures 4 and 5), which is consistent with the response of the analytical ZBP model to increasing mixing strength. Figure 4 illustrates the resolution-dependent behavior of cloud fraction, atmospheric cloud radiative effects (ACRE), relative humidity, and the distribution of column-integrated ice-water path. ACRE is defined as the difference between the actual radiative heating rate profile and the hypothetical clear-sky radiative heating rate profile which assumes no cloud condensate. Both the SAM1MOM and Morrison et al. (2005) simulations exhibit a rise in relative humidity throughout the entire free troposphere and an increase of high cloud fraction with finer resolution. A grid is classified as cloudy if the cloud mass (the sum of ice and liquid water) mixing ratio exceeds 10^{-5} kg kg^{-1}. As the grid spacing decreases from 4 km to 125 m, the peak anvil cloud fraction increases from 7.5% to 13% in the SAM1MOM simulations (Figure 4a) and from 17% to 27% in the Morrison et al. (2005) simulations (Figure 4e). This amplified cloud fraction subsequently leads to increased atmospheric cloud radiative heating (ACRE) throughout most of the free troposphere (Figures 4b and 4f). The histogram of ice-water path shows that the cloud amount increase is primarily contributed by the more frequent occurrence of columns with ice-water path of near 0.01–0.1 kg m^{-2} (Figures 4d and 4h). Hu et al. (2021) (their Figure 9) showed that this range of ice-water path corresponds to optically thin clouds and has a heating effect for the troposphere, consistent with the ACRE changes. In Figure S2 in Supporting Information S1, we also present cloud mixing ratio profiles, showing both domain-mean values and averages over cloudy grids only. For both microphysics schemes, increasing the model resolution tends to decrease the liquid cloud mixing ratio, both in the domain mean and in the cloudy-grid mean, while simultaneously reducing the low cloud fraction (Figures 4a and 4e).

The increase in anvil cloud fraction can be related to the increasing convective updraft mass flux. Anvil cloud fraction can be diagnosed as the product of mass detrainment and cloud lifetime (e.g., Beydoun et al., 2021; Seeley et al., 2019). In Figure 5, we present profiles of convective updraft mass flux and in-cloud sedimentation flux divergence to look at the change of mass detrainment and lifetime change. The convective updraft is characterized by grids with a vertical velocity greater than 1 m s^{-1} and a cloud mixing ratio exceeding 10^{-5} kg kg^{-1}. Changing the velocity threshold to be greater than 0 or further including convective downdraft still shows a qualitatively similar trend of increasing mass flux (Figure S3 in Supporting Information S1). The in-cloud sedimentation flux divergence is defined as dqc_{sed}/qc averaged over cloudy grids, where qc is the cloud mass (ice plus liquid water) mixing ratio and dqc_{sed} is the tendency of qc due to sedimentation of cloud ice. This sedimentation flux divergence is the major term of the net removal rate in Beydoun et al. (2021) and could be interpreted as one over lifetime. Sedimentation flux divergence is positive above approximately 10 km and negative below, representing cloud ice falling from the detraining level downwards. In both the SAM1MOM and Morrison et al. (2005) simulations, the convective updraft mass flux at above 11 km increases with higher resolution, signifying an increased vertical mass convergence above this altitude. By mass continuity, the increase of
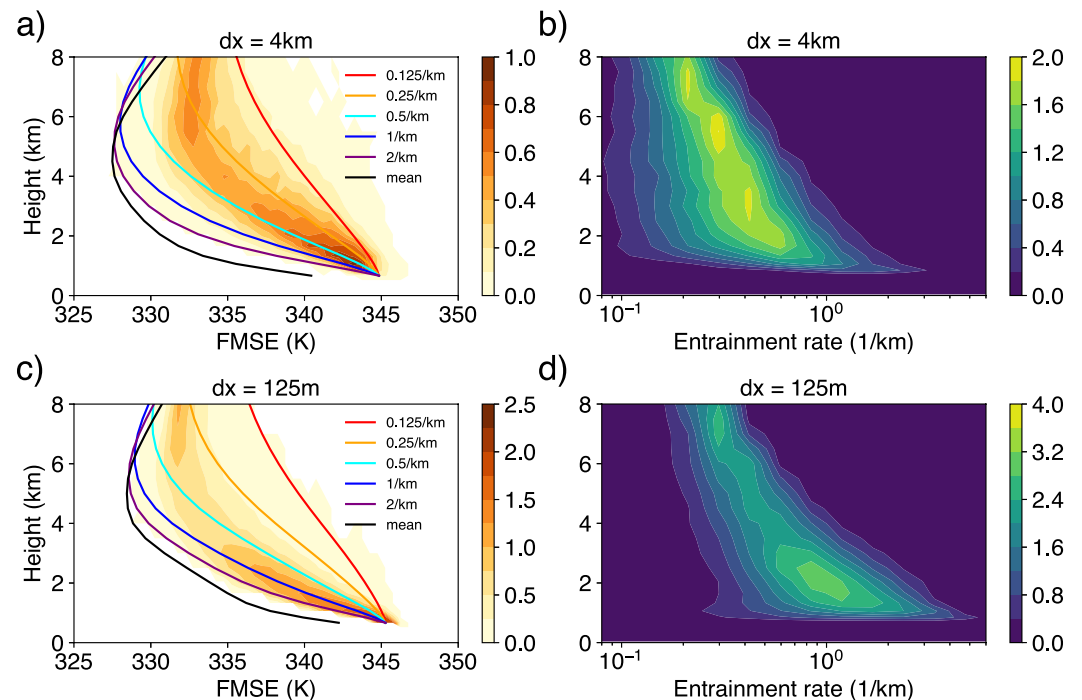
Figure 3. The distribution of convective updraft mass flux in FMSE-height space (left column) and in entrainment-height space (right column) for grid size of 4 km (upper row) and 125 m (lower row). In the left column, we show the mass flux distribution (with a unit of $kg\,m^{-2}\,s^{-1}\,bin^{-1}$) binned by their frozen moist static energy (FMSE) (in unit of K). There are 50 bins with 0.5 K intervals between 325 and 350 K. The individual lines represent the FMSE profiles of entraining plumes rising from the cloud base with different entrainment rates, except the black line which represents domain-mean FMSE profiles. In the right column, we show the mass flux distribution (with a unit of $kg\,m^{-2}\,s^{-1}\,bin^{-1}$) binned by their effective entrainment rate. The bin boundaries have entrainment rates of $2^{(i/2)-4}$, for $i = 0, 1, 2, \ldots, 16$, with a unit of km^{-1}. We calculated the instantaneous FMSE profiles with these different entrainment rates and binned the mass flux according to these FMSE profiles. For example, all the mass flux between the cyan and blue lines in the left panels will be counted as having entrainment rate between 0.5 and 1 km^{-1} in the right panels.

vertical convective mass flux convergence corresponds to an increase of mass detrainment and an increase of horizontal mass convergence in the clear-sky region. The convective updraft mass flux in the middle and lower troposphere shows non-monotonic change. This may be partly due to increased ACRE with finer resolution (e.g., see Figure A3 and the corresponding discussion in Appendix A). The sedimentation rate is weaker at finer resolutions in the SAM1MOM scheme but is slightly stronger in the Morrison et al. (2005) scheme. Hence, the observed increase in cloud fraction with finer resolution in both SAM1MOM and Morrison et al. (2005) simulations is predominantly driven by the amplification of mass detrainment. The contribution from lifetime changes is less certain and could be contingent on the microphysics schemes employed.

4.3. Budgets for Environmental Subsidence

In this section, we investigate the mechanisms responsible for the increase in convective updraft mass flux associated with finer resolutions. Because of mass continuity, the mass flux in convective updrafts must be in balance with subsidence in the surrounding environment, which we define as grids possessing a cloud mixing ratio less than $10^{-5}\,kg\,kg^{-1}$. We shall use dry static energy budget to gain some understanding of changes to environmental subsidence. By employing the dry static energy budget of the environment, we decompose the subsidence and will demonstrate that modifications to mass flux profiles could be attributed to changes in both cloud evaporation rate and entrainment rate. In reality, the changes in cloud evaporation and in entrainment rate are not purely independent as the change of horizontal mixing can influence both of them.

The dry static energy is defined as $s = c_p T + gz$. The budget equation for dry static energy is given by
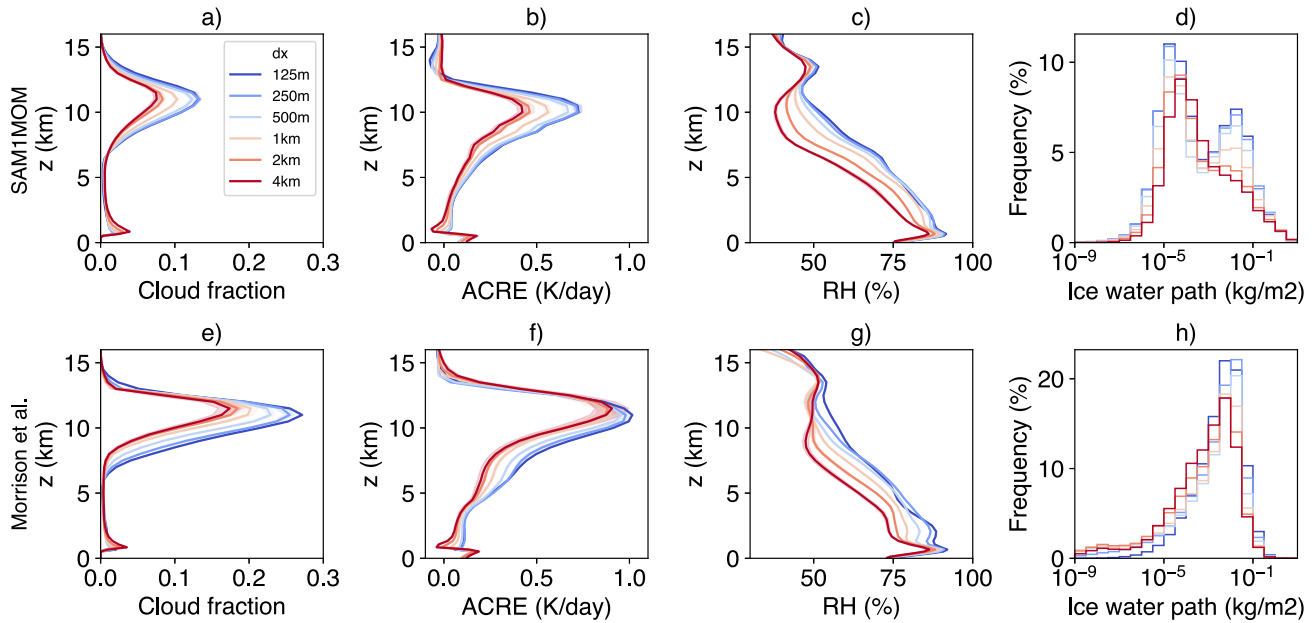
Figure 4. Domain-mean steady-state profiles of cloud fraction (left column), atmosphere cloud radiative effects (the second column), and relative humidity (the third column). The last column shows the histogram of column integrated ice-water path. The upper row corresponds to the SAM1MOM simulations, while the lower row represents the Morrison et al. (2005) simulations. Different colors indicate varying grid sizes, with warmer colors denoting coarser resolutions. Shaded uncertainty range is estimated as the standard deviation of time-mean profiles of each non-overlapping 2.5-day time block.

$$\frac{\partial s}{\partial t} + \vec{u} \cdot \nabla_h s + w \frac{\partial s}{\partial z} = Q_{rad} + Q_{lat} \tag{5}$$

where Q_{rad} is the radiative heating, and Q_{lat} is the latent heating in the environment. By averaging over all environmental grids and time, and ignoring the time tendency, we obtain:

$$\langle \vec{u} \cdot \nabla_h s \rangle + \langle w \frac{\partial s}{\partial z} \rangle = \langle Q_{rad} \rangle + \langle Q_{lat} \rangle \tag{6}$$

After further decomposition of $\langle w \frac{\partial s}{\partial z} \rangle = \langle w \rangle \langle \frac{\partial s}{\partial z} \rangle + \langle w' \frac{\partial s'}{\partial z} \rangle$, the averaged environmental subsidence can be expressed as:

$$\langle w \rangle = \frac{\langle Q_{rad} \rangle}{\langle \frac{\partial s}{\partial z} \rangle} + \frac{\langle Q_{lat} \rangle}{\langle \frac{\partial s}{\partial z} \rangle} - \frac{\langle \vec{u} \cdot \nabla_h s \rangle}{\langle \frac{\partial s}{\partial z} \rangle} - \frac{\langle w' \frac{\partial s'}{\partial z} \rangle}{\langle \frac{\partial s}{\partial z} \rangle} \tag{7}$$

This equation encapsulates the energy balance within the environment, implying that the subsidence heating is counterbalanced by the cooling induced by radiation and phase changes in water. In Figure 6, we show the profiles of latent-driven and radiation-driven subsidence for the SAM1MOM simulations. The combined effect of latent- and radiation-driven subsidence closely mirrors the subsidence deduced from model output, and the contribution of advection terms appears minor in comparison to the contribution of radiation and latent heating (not shown).

The subsidence near the anvil level increases with finer resolution (Figure 6a), which is consistent with the change of convective updraft mass flux. In the SAM1MOM simulations, a large portion of the increasing subsidence is counteracted by the negative latent heating in the environment due to evaporation and sublimation of clouds (Figure 6b). Conversely, negative radiative heating accounts for a relatively smaller portion of this balance (Figure 6c). The relative contribution of latent and radiative heating in the Morrison et al. (2005) scheme is somewhat different. We will probe into the nuances of the Morrison et al. (2005) simulations later in this section. It is important to underscore that the role of latent heating can be influenced by the specific definition of "environment."
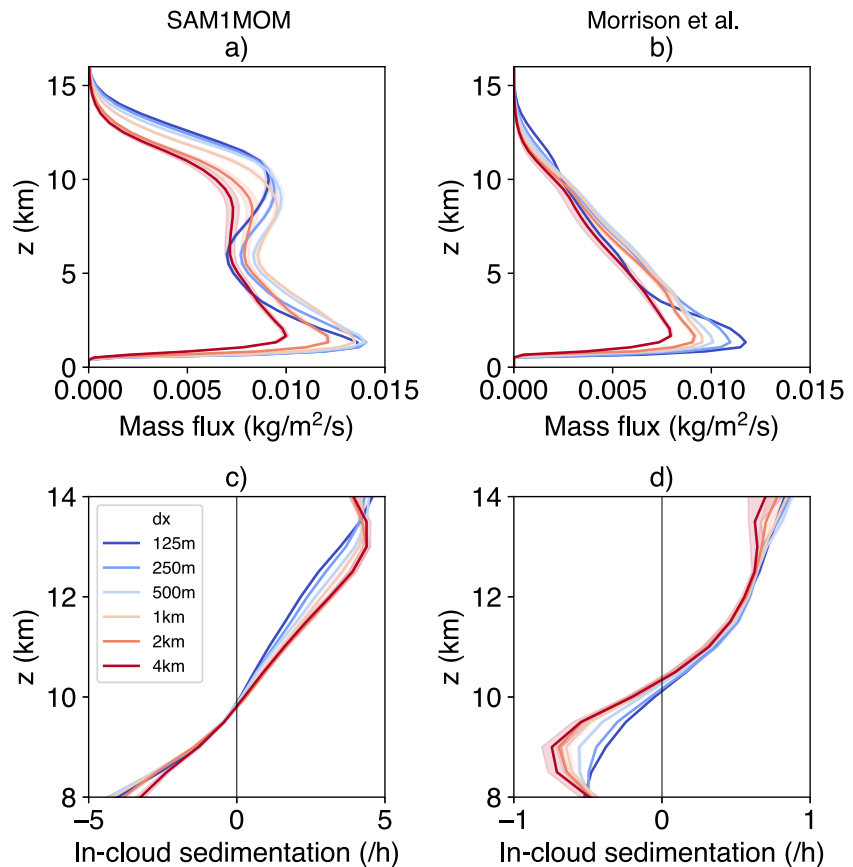
Figure 5. Domain-mean steady-state profiles of convective updraft mass flux (upper row) and cloud ice sedimentation rate (lower row). The left column corresponds to the SAM1MOM simulations, while the right column represents the Morrison et al. (2005) simulations. Different colors indicate varying grid sizes, with warmer colors denoting coarser resolutions. Shaded uncertainty range is estimated as the standard deviation of time-mean profiles of each non-overlapping 2.5-day time block.

In our study, the environment, defined as grids with a cloud mixing ratio less than 10^{-5} kg kg^{-1}, incorporates grids distanced from clouds as well as those near clouds, which experience evaporation and sublimation. Results in the following paragraphs are not sensitive to the choice of cloud threshold. Changing the threshold from 10^{-5} kg kg^{-1} to 10^{-7} kg kg^{-1} results in minimal change. Such insensitivity might be attributed to the model's time-splitting procedure, where evaporation is calculated before the output of the cloud mixing ratio. Consequently, grid cells can reflect marginal cloud mixing ratios while still indicating evaporation in the resultant data.

The change of latent-driven subsidence is consistent with the change of latent heating in the environment (Figure 6d). In the upper troposphere, the cooling from phase change is primarily associated with cloud evaporation/sublimation (Figure 6e). For simplicity, we will henceforth use the term "evaporation" to refer to both the evaporation of cloud water and the sublimation of cloud ice. The cooling due to re-evaporation of precipitation, which is not displayed here, is less significant than that of clouds in the upper troposphere, although it presents a similar strength in the lower troposphere. We have shown that a finer resolution model tends to generate more clouds and updraft mass flux. Therefore, the observed increase in latent cooling might be simply a consequence of the larger amount of clouds available for evaporation. However, an interesting observation arises when we normalize the cooling due to cloud evaporation by the domain mean cloud mass mixing ratio (Figure 6f). Domain mean cloud mixing ratio is proportional to the total cloud mass in each layer. It becomes evident that, per unit mass, clouds tend to induce a greater amount of cooling in the environment when modeled at finer resolution.

The observed enhancement in evaporation could be associated with the model resolution through the geometric representation of cloud boundaries. We will use clouds at the anvil level as an example, but we assume the
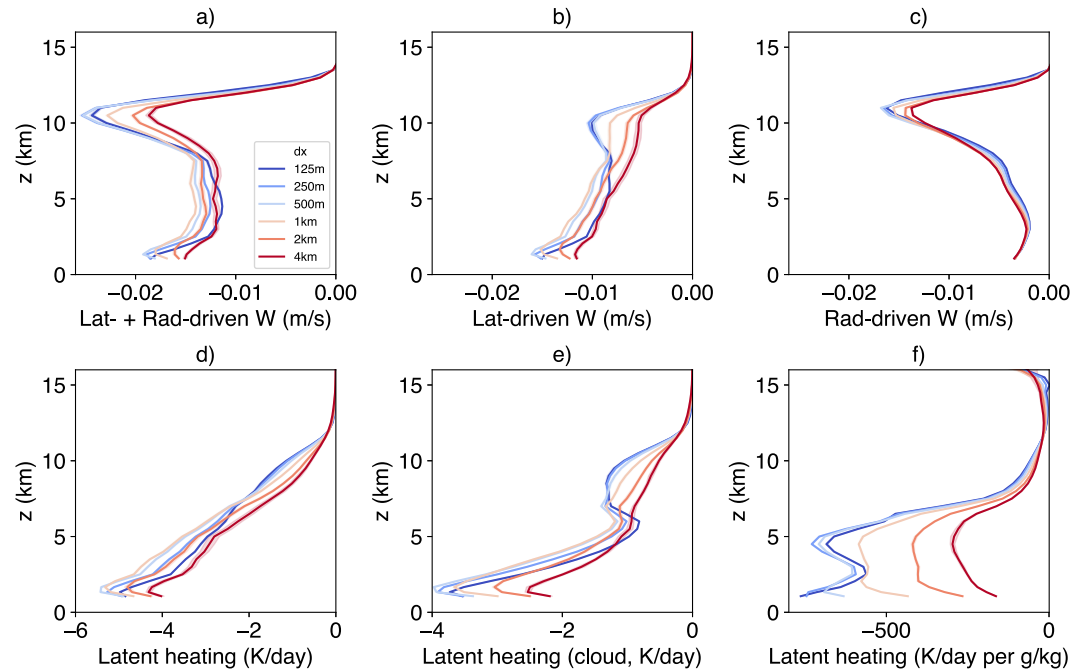
Figure 6. Energy budget for environmental subsidence for the SAM1MOM simulations. The first row shows the subsidence contributed by latent heat (panel b), by radiative cooling (panel c), and by both (a). Panel (d) shows the latent heating rate averaged in environments. Panel (e) shows the latent heating rate associated with the phase change between clouds and vapor averaged in environments. Panel (f) normalizes the cloud-related latent heating rate in panel (e) by the domain-mean cloud mixing ratio. Shaded uncertainty range is estimated as the standard deviation of time-mean profiles of each non-overlapping 2.5-day time block.

intuition behind should apply to clouds at all levels. Horizontal snapshots of the cloud mixing ratio at an altitude of $z = 10$ km are depicted in Figures 7a and 7b. These images represent two 32 km × 32 km subdomains in the 4 km-resolution and 125 m-resolution simulations respectively. When compared to the clouds in the coarser 4 km-resolution simulation, the clouds in the 125 m-resolution simulation exhibit more complex boundary structures and tend to be more dispersed. As a result, clouds modeled at finer resolutions exhibit a higher perimeter area ratio (Figure 7c). In other words, for a cloud patch of the same area, the total perimeter will be longer in the simulation with finer resolution. This effect is somewhat analogous to the coastline paradox in fractal geometry, where the measured length of a coastline varies depending on the scale of measurement. The increased perimeter-to-area ratio exposes a larger mass of the cloud to the environment, potentially leading to greater evaporation near the cloud edges.

Siebesma and Jonker (2000) explored the fractal nature of cumulus clouds in Large-Eddy Simulations. They argued that while a coarse grid will underestimate cloud surface area, the total sub-grid turbulent transport could become resolution-independent if the grid size is within the inertia subrange. However, in our simulations with a grid size on the order of 1 km, sub-grid diffusion in the free troposphere is minimal. We observed that turning off horizontal sub-grid diffusion of scalars (such as energy and water) resulted in only minor changes to the profiles of cloud fraction and environmental evaporation (not shown). The cloud evaporation of deep convection is substantially influenced by numerical diffusion and can be enhanced by a larger perimeter-to-area ratio. To illustrate this point, similar to Equation 8 in Jeevanjee and Zhou (2022), we derived an equation (see Appendix B for complete derivation) that describes the relationship between cloud evaporation in relation to resolved advection and the perimeter-to-area ratio:

$$\frac{Q_{\text{lat,env}}}{q_{\text{m}}} = \frac{L}{A} U_{\text{adv}} \frac{q_{\text{c,edge}} + q_{\text{v,env}}^*(1 - \mathcal{R})}{q_{\text{cld}}} \frac{L_{\text{v}}}{2c_p f_{\text{env}}} \tag{8}$$
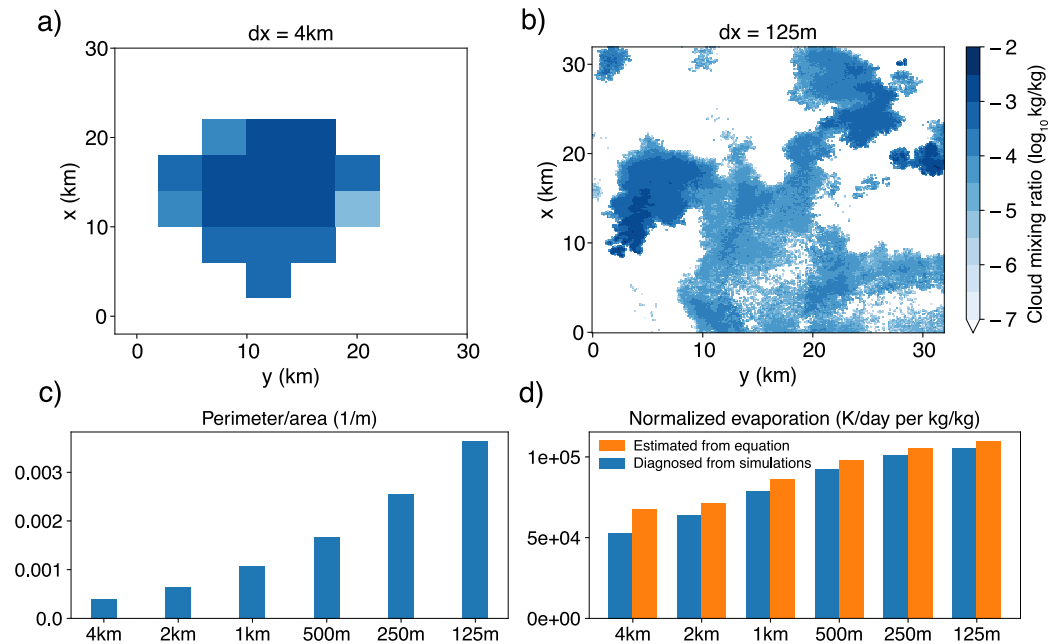
Figure 7. The upper row shows the cloud mixing ratio snapshots at $z = 10$ km in a 32 km $\times$ 32 km subdomain in the SAM1MOM simulations with grid size of 4 km (a) and 125 m (b). Panel (c) shows the perimeter area ratio in the SAM1MOM simulations with different grid sizes. Panel (d) shows the normalized evaporation in Figure 6f at $z = 10$ km. Blue bars are direct model diagnostic values, and orange bars are estimated by Equation 8.

Equation 8 indicates that the evaporation due to horizontal mixing at cloud edges is dependent on several factors. These include the perimeter-to-area ratio (L/A), the resolved horizontal velocity near the cloud edge (U_{adv}), the cloud mixing ratio near the cloud edge ($q_{\mathrm{c,edge}}$), the saturation deficit in the environment $\left(q_{\mathrm{v,env}}^{*}(1 - \mathcal{R})\right)$, and the average cloud mixing ratio within cloudy grids (q_{cld}). We verify this equation at the anvil level, characterized by relatively weak vertical motion near the cloud edge, hence, making cloud evaporation predominantly attributable to horizontal mixing. Figure 7d demonstrates that the diagnosed evaporation using Equation 8 qualitatively aligns with the direct model output. From this equation, it is evident that an increased perimeter-to-area ratio can positively contribute to enhanced cloud evaporation. In Appendix A, we delve into how other terms in Equation 8 vary with model resolution. It is more difficult to validate Equation 8 at lower levels. In the middle troposphere, clouds are typically very close to the convective core, and evaporation/condensation associated with vertical motion may not be neglected. However, we assume the enhanced horizontal mixing and larger perimeter area ratio should still positively contribute to the enhanced evaporation we show in Figure 6f. It is important to note the importance of enhanced horizontal mixing occurring at all levels, not solely at the anvil level. More efficient evaporation at lower levels could contribute to mass flux increase at those levels and, by mass continuity, should have a continuing influence on mass flux at higher levels (Jeevanjee & Zhou, 2022).

In the Morrison et al. (2005) simulations, consistent with the mass flux change, we also observe an enhancement in subsidence near the anvil level, as shown in Figure 8a. However, the contribution from latent-driven subsidence (Figure 8b) is weaker in the Morrison et al. (2005) scheme compared to the SAM1MOM scheme. Primarily, the subsidence change near the anvil level is dominated by radiation-driven subsidence (see Figure 8c). We further dissect the radiation-driven subsidence into radiation and stability components. The radiative cooling shows slight non-monotonic changes (Figure 8d), while the upper troposphere is less stable with finer resolution (Figures 8e and 8f). The change in stability could be associated with the shift in the entrainment rate (Figure 3), which tends to increase with finer resolution.

Morrison et al. (2005) simulations reveal the stability pathway that is similar to the behavior of the ZBP model with a small evaporation parameter μ. The similarity here primarily comes from the diminishing evaporation in the upper troposphere. However, given the complexity of the SAM1MOM and Morrison microphysics schemes, it is hard to attribute their difference to a single parameter like μ or a single microphysical process. It is important
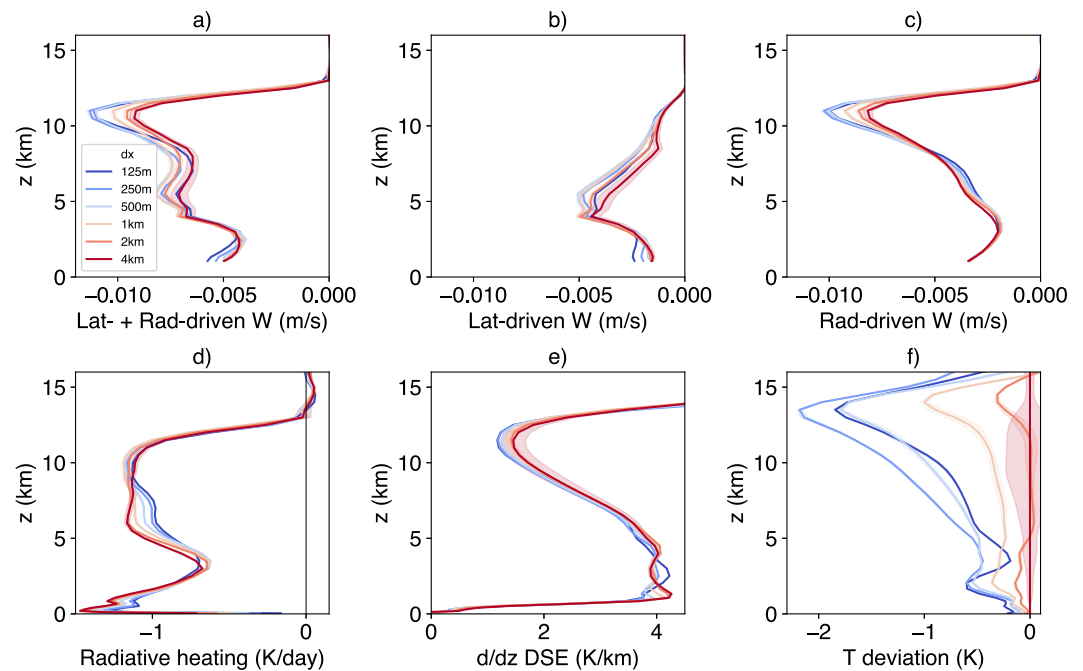
Figure 8. Energy budget for environmental subsidence for the Morrison et al. (2005) simulations. The first row shows the subsidence contributed by latent heat (panel b), by radiative cooling (panel c), and by both (a). Panel (d) shows the radiative heating rate averaged in environments. Panel (e) shows the vertical gradient of dry static energy averaged in environments. Panel f shows the absolute temperature profiles as deviation to the 4 km Morrison et al. (2005) simulation. Shaded uncertainty range is estimated as the standard deviation of time-mean profiles of each non-overlapping 2.5-day time block.

to clarify that we do not intend to use the low evaporation parameter case in the ZBP model to directly explain the resolution sensitivity observed in the Morrison et al. (2005) simulations. Rather, the ZBP model results are meant to illustrate potential pathways and mechanisms by which entrainment can influence upper-level clear-sky convergence and net detrainment.

Figure 9 explores the reasons behind the distinctive environmental energy balance regime observed in the Morrison et al. (2005) simulations compared to the SAM1MOM simulations. In the Morrison et al. (2005) simulations, the cooling effect from evaporation in the upper troposphere is notably weaker than that from radiation. Two factors could contribute to this subdued evaporation: diminished updrafts and a slower evaporation rate. As previously noted, the Morrison et al. (2005) scheme tends to generate more anvil clouds, likely due to the significantly slower ice sedimentation removal rate and prolonged lifetime (refer to Figure 5). The enhanced cloud radiative heating in the Morrison et al. (2005) simulations could stabilize the upper troposphere, thereby reducing the intensity of updrafts. When we disable cloud-radiation interactions in the Morrison et al. (2005) simulations (represented by solid lines in Figure 9), we observe an increase in upper troposphere convective updrafts and stronger latent-driven subsidence, compared to the default Morrison et al. (2005) simulations (dotted lines in Figure 9). Additionally, the Morrison et al. (2005) scheme does not employ saturation adjustment for cloud ice, potentially slowing evaporation compared to the SAM1MOM scheme. When we deactivate the cloud-radiation interactions and accelerate the cloud ice sublimation rate 100 times to mimic the saturation adjustment (dashed lines in Figure 9), the result is faster evaporation and intensified updrafts. Consequently, latent-driven subsidence now contributes comparably to radiation-driven subsidence in modifying total subsidence near the anvil level as resolution becomes finer (see Figures 9b–9d).

5. Conclusions and Discussion

In this work, we study how mixing between convective updraft plumes and the environment can influence the macro-scale equilibrium atmospheric state, especially upper troposphere convective mass flux and anvil clouds. We first use an analytical simple model called the ZBP model to illustrate qualitatively how small-scale processes like plume-environment mixing and evaporation rate can influence the large-scale vertical temperature and
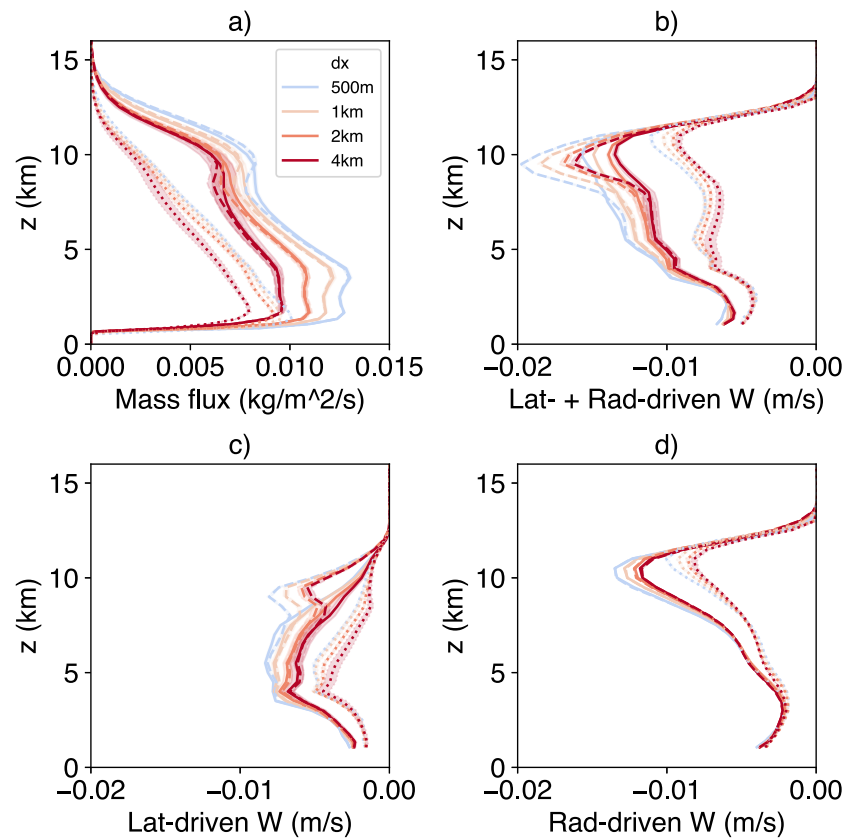
Figure 9. Convective updraft mass flux and energy budget for environmental subsidence in modified Morrison et al. (2005) simulations. Solid lines represent simulations where cloud-radiation interactions are deactivated. Dashed lines indicate simulations with both cloud-radiation interactions deactivated and expedited cloud ice sublimation. Dotted lines represent default Morrison et al. (2005) simulations. Panel a displays the convective updraft mass flux. Panels (b–d) present the subsidence contributions from latent heat (panel c), radiative cooling (panel d), and a combination of both (panel b). Shaded uncertainty range is estimated as the standard deviation of time-mean profiles of each non-overlapping 2.5-day time block.

moisture structure and convective mass flux. With the ZBP model, we find that increasing mixing strength can lead to an increase in upper-troposphere mass flux through two pathways based on clear-sky energy balance, either through more cloud evaporation cooling in the environment or through weaker atmospheric stability. We further tested these pathways in numerical simulations of RCE by increasing the horizontal resolution from 4 km to 125 m with a fixed domain size. We found both pathways in the RCE simulations with two different microphysics schemes, a single-moment scheme and a double-moment Morrison et al. (2005) scheme. Which pathway dominates may depend on the relative magnitude of environmental cloud evaporation cooling versus radiative cooling in the upper troposphere. When the evaporation cooling is much weaker than the radiative cooling (as in the Morrison et al. (2005) simulations or with small evaporation parameter in the ZBP model), the stability pathway dominates, which is a new finding compared to a previous study (Jeevanjee & Zhou, 2022). It should be noted that the ZBP model serves to highlight potential pathways and mechanisms rather than directly explaining the simulation results. The different dominant pathways observed in the simulations using the two different microphysics schemes should not be simply attributed to the evaporation parameter in the ZBP model. Instead, the ZBP model results are meant to illustrate the potential mechanisms by which entrainment can influence upper-level clear-sky convergence and net detrainment. Given the complexity of the two microphysics schemes, attributing their differences to a single evaporation parameter or a single microphysical process is challenging.

One innovation of this study is the refinement of the ZBP model to get self-consistent mass flux solutions. As described in Section 2, previous studies on the ZBP model such as Singh and Neogi (2022) and Romps (2021) have an inconsistency issue of their mass flux solution and assumptions of equal entrainment rate and detrainment rate. By treating the detrainment rate as an unknown variable instead of a parameter and utilizing the RCE concept

to determine the boundary condition for mass flux, we can achieve a self-consistent mass flux solution in our refined ZBP model. This ZBP can provide a simple framework to understand the equilibrium state atmosphere and the interaction between small-scale processes to large-scale atmosphere properties, as illustrated in this study and many previous studies (Romps, 2014, 2021; Singh & Neogi, 2022; Singh et al., 2019). While we have only used this refined ZBP model with zero large-scale vertical motion, one could extend this refined ZBP model to include nonzero vertical motion to account for the effect of large-scale circulation and interaction between tropical ascent region and dry subsidence region as in Singh and Neogi (2022) and Romps (2021). Another future direction would be to extend the ZBP model to include the boundary layer. Currently, the ZBP model only solves the atmospheric profiles in the free troposphere and requires boundary conditions at the cloud base. Potentially, it is possible to use boundary layer equilibrium assumptions so that the model only requires surface boundary conditions. Additionally, the microphysics included in the ZBP model are highly simplified. Incorporating the effects of sedimentation, precipitation re-evaporation, and ACRE could allow for a more realistic representation, even for an idealized RCE atmosphere.

In this study, we use varying horizontal resolutions as a proxy for different plume-environment mixing strengths. One needs to be more careful to infer the general resolution dependence of km-scale or hm-scale convection-permitting simulations. First, the dependence of mixing strength on model resolution can depend on the specific subgrid-scale scheme and advection scheme used in a model. In the case where parameterized sub-grid diffusion is much weaker than the numerical diffusion (as in our simulations), the choice of numerical scheme and the representation of numerical diffusion could potentially matter for large-scale simulation properties and may warrant further study. Second, our study did not consider any large-scale convective organization, which is common in more realistic large-domain RCE simulations or global storm-resolving simulations. It is unclear how small-scale mixing could change the large-scale convective organization, which can be important for the sensitivity of large-scale thermal properties (e.g., Becker et al., 2017). In addition, we only changed the horizontal resolution in this study and fixed the vertical resolution. Previous studies (e.g., Jenney et al., 2023; Ohno & Satoh, 2018; Ohno et al., 2019) have shown that the vertical resolution can also influence the mass flux and anvil cloud fraction. In the numerical model we use, some preliminary experiments of increasing vertical resolution (not shown) yielded results similar to Jenney et al. (2023) and suggest a counter-effect on anvil cloud fraction and mass flux compared to increasing horizontal resolution. How the cloud and mass flux respond to increasing both horizontal and vertical resolution may depend on how the strength of mixing changes, which could again depend on the subgrid-scale scheme and advection scheme. Besides spatial resolution change, temporal resolution could also play a role, but we have not fully quantified its impact. The effective time step is smaller with finer resolution to satisfy the Courant–Friedrichs–Lewy condition. For the one-moment microphysics scheme, a smaller time step means that the instantaneous saturation adjustment also happens faster. Lastly, this study focuses on the equilibrium state of an atmosphere. Sensitivities of simulations of transient convective systems on resolution or the strength of mixing could be very different.

In addition to the sensitivity of mass flux and anvil cloud fraction on mixing strength and resolution, we also noticed a large sensitivity of anvil cloud fraction on the microphysics scheme. Previous studies (e.g., Hu et al., 2021; Powell et al., 2012) have found that the Morrison et al. (2005) microphysics scheme tends to produce excessive anvil cloud fraction. It is worth further future study to better understand the sensitivity of anvil cloud amount on microphysics schemes and different microphysical processes.

Appendix A: Refined Solutions of a Zero-Buoyancy Plume Model

Here we document the details of how we solve the ZBP model to get self-consistent solutions about steady-state mass flux, detrainment rate, and other atmosphere profiles. Following Singh and Neogi (2022), the equations we solve are:

$$\frac{\partial M_c}{\partial z} = e - d \tag{A1}$$

$$M_c + M_e = 0 \tag{A2}$$

$$\frac{\partial (M_c q^*)}{\partial z} = eq - dq^* - s_{cond} \tag{A3}$$

$$\frac{\partial(M_e q)}{\partial z} = dq^* - eq + s_{\text{evap}} \tag{A4}$$

$$\frac{\partial(M_c h^*)}{\partial z} = eh - dh^* \tag{A5}$$

$$\frac{\partial(M_e h)}{\partial z} = dh^* - eh + Q_{\text{rad}} \tag{A6}$$

$$h^* - h = L_v(q^* - q) \tag{A7}$$

$$s_{\text{evap}} = \mu d(q^* - q) \tag{A8}$$

$$\frac{\partial p}{\partial z} = -\frac{pg}{R_d T} \tag{A9}$$

Equations A1 and A2 are mass conservation equations. M_c is the mass flux of convective updrafts, and M_e is mass flux in the environment. We assume there is no large-scale advection, so the net mass flux in updrafts and the environment is 0. e is mass entrainment, and d is mass detrainment. Fractional entrainment rate ϵ and fractional detrainment rate δ are defined as:

$$\epsilon = e/M_c \tag{A10}$$

$$\delta = d/M_c \tag{A11}$$

Equations A3 and A4 describe the water vapor conservation in the updraft plume and the environment separately. q is the specific humidity in the environment. q^* is the saturation specific humidity in the updraft plume, which is simply a function of temperature and pressure:

$$q^* = 0.622 p_v^*/p = 0.622\frac{p_0}{p}e^{-\frac{L_v}{R_v T}} \tag{A12}$$

where $p_v^* = p_0 \exp(-L_v/(R_v T))$ is the saturation vapor pressure, $L_v = 2.51\text{e}6$ J kg^{-1} is the latent heat of condensation, $R_v = 461$ J kg^{-1}K^{-1} is gas constant for water vapor, $p_0 = 2.69\text{e}11$ Pa is a constant.

Equations A5 and A6 describe the conservation of moist static energy in the updraft plume and the environment. $h = c_p T + gz + L_v q$ is the moist static energy in the environment, and $h^* = c_p T + gz + L_v q^*$ is the saturation moist static energy in the updraft plume. We specify radiative heating rate to be simply a function of temperature,

$$Q_{\text{rad}}/(c_p \rho) = \begin{cases} Q_0, & \text{if } T > 250K \\ Q_0(0.5 + 0.5\cos(\pi(250 - T)/(250 - 200))), & \text{if } 250K > T > 200K \\ 0, & \text{if } T < 200K \end{cases} \tag{A13}$$

where $Q_0 = -1\text{K day}^{-1}$. Radiative heating rate is constantly -1K day^{-1} in the lower and middle troposphere and gradually decays to 0 from $T = 250$ K to $T = 200$ K. $\rho = p/R_d T$ is the air density. It is worth noting that Equation A13 ignores the positive radiative heating often observed in the tropopause layer (e.g., Figure S1a in Supporting Information S1) associated with deep convective overshoots.

Equation A7 implies the zero-buoyancy assumption that the temperature in updrafts is the same as the temperature in the environment at the same height. Figure S1b in Supporting Information S1 shows that the time-averaged buoyancy in the convective updraft in our cloud-resolving numerical simulations is within 1 K except at the top of the troposphere above 14 km. At higher altitudes, Equation A7 is not a good assumption as deep convective overshoots are infrequent and the stratification becomes gradually decoupled from deep convection.

Equation A8 is the parameterization of cloud evaporation in the environment, following the definition in the Singh and Neogi (2022). μ is a unitless parameter that controls the speed of cloud evaporation. We assume cloud

evaporation happens at the level where clouds are condensed, and we assume there is no evaporation of precipitation. Equation A9 is the hydrostatic balance, and $R_d = 287\,\text{J kg}^{-1}\text{K}^{-1}$ is the gas constant for dry air. Figure S1c in Supporting Information S1 demonstrates that the domain-mean profiles in cloud-resolving numerical simulations follow the hydrostatic balance well.

For Equations A1–A9, there are 9 equations but 11 unknown variables: M_c, M_e, ϵ, δ, q^*, q, h, s_{cond}, s_{evap}, μ, and p. We have excluded h^* and Q_{rad} from unknown variables since they can be expressed using T and p through Equations A12 and A13. We take ϵ and μ to be the free parameters that we can specify, and the rest of the equations is just enough to get a self-consistent solution. If one further specifies δ, then there will be more equations than unknown variables, in which case there cannot be the self-consistent solution. Next, we will describe how we solve these equations as an ODE problem and express the equations as $\frac{\partial}{\partial z}(M_c, p, q, T) = F(M_c, p, q, T)$.

Replacing Equation A1 into Equations A3–A7, we can get:

$$M_c \frac{\partial q^*}{\partial z} = -\epsilon(1 - \mathcal{R})M_c q^* - s_{cond} \tag{A14}$$

$$M_e \frac{\partial q}{\partial z} = \delta(1 + \mu)(1 - \mathcal{R})M_c q^* \tag{A15}$$

$$M_c \frac{\partial h^*}{\partial z} = -\epsilon L_v(1 - \mathcal{R})M_c q^* \tag{A16}$$

$$M_e \frac{\partial h}{\partial z} = \delta L_v(1 - \mathcal{R})M_c q^* + Q_{rad} \tag{A17}$$

$\mathcal{R} = q/q^*$ is the relative humidity in the environment.

Equation A1 can be rewritten as:

$$\frac{\partial M_c}{\partial z} = M_c(\epsilon - \delta) \tag{A18}$$

Using Equations A2 and A15, we get:

$$\frac{\partial q}{\partial z} = -\delta(1 + \mu)(1 - \mathcal{R})q^* \tag{A19}$$

Equation A16 can be used to express the temperature lapse rate $\Gamma = -\frac{\partial T}{\partial z}$. From the definition of h^*, we have:

$$\frac{\partial h^*}{\partial z} = -c_p\Gamma + g + L_v\frac{\partial q^*}{\partial z} \tag{A20}$$

Using Equations A9 and A12 and defining $\gamma = -(1/q^*)\frac{\partial q^*}{\partial z}$, we can get:

$$\gamma = \frac{L_v\Gamma}{R_v T^2} - \frac{g}{R_d T} \tag{A21}$$

Replacing Equations A20 and A21 into Equation A16, we can get:

$$\frac{\partial T}{\partial z} = -\Gamma_m - \frac{\epsilon L_v(1 - \mathcal{R})q^*}{c_p + q^* L_v^2/(R_v T^2)} \tag{A22}$$

where

$$\Gamma_m = \frac{g\left(1 + \frac{L_v q^*}{R_d T}\right)}{c_p + q^* L_v^2/(R_v T^2)}$$

is the moist adiabatic lapse rate when the fractional entrainment rate $\epsilon = 0$.

By replacing the Γ in Equation A21 with Equation A22, we can also rewrite γ as:

$$\gamma = \gamma_m + \epsilon b(1 - \mathcal{R}) \tag{A23}$$

where

$$\gamma_m = \frac{L_v \Gamma_m}{R_v T^2} - \frac{g}{R_d T}$$

is the fractional saturation specific humidity gradient along a moist adiabat, and

$$b = \frac{q^* L_v^2}{q^* L_v^2 + c_p R_v T^2}$$

is a nondimensional residual term.

When we sum Equations A3 and A4, sum Equations A5 and A6, and use Equations A2 and A7, we can get the energy balance equation:

$$Q_{\mathrm{rad}} = -L_v (s_{\mathrm{cond}} - s_{\mathrm{evap}}) \tag{A24}$$

Replacing Equations A8 and A14 into Equation A24, we can get the expression of δ:

$$\delta = -\frac{\epsilon(1 - b)}{\mu} + \frac{\gamma_m}{\mu(1 - \mathcal{R})} + \frac{Q_{\mathrm{rad}}}{\mu(1 - \mathcal{R}) q^* L_v M_c} \tag{A25}$$

Now with Equations A9, A18, A19, A22, and A25, we have the closed form expression for our ODE problem:

$$\frac{\partial}{\partial z}(M_c, p, q, T) = F(M_c, p, q, T) \tag{A26}$$

where the right-hand side only depends on M_c, p, q, and T. Given boundary conditions at cloud base (we use $z = 500$ m), Equation A26 can integrate upwards and get the full atmosphere profiles. It is worth noting that Equation A25 is singular if $\mu = 0$. We will discuss the solution for that case later in this section.

For boundary conditions, we specify a surface temperature of 303 K and surface pressure of 10^5 Pa. We assume a dry adiabatic lapse rate of $g/c_p = 9.8$ Kkm^{-1} below the cloud base, and we can use Equation A9 to integrate pressure p from the surface to the cloud base. For environmental specific humidity q at the cloud base, we do not have a solid constraint. If one assumes $\frac{\partial q}{\partial z} \approx \mathcal{R} \frac{\partial q^*}{\partial z}$ (the vertical gradient of RH is much smaller than the vertical gradient of q^*), Equation A15 can reduce to:

$$\mathcal{R} = \frac{\delta(1 + \mu)}{\delta(1 + \mu) + \gamma} \tag{A27}$$

We determine our cloud base q using Equation A27, and the value of δ in Equation A27 is taken from the ϵ. In this way, we implicitly assume that increasing ϵ or μ can have a moistening effect at the cloud base, which intuitively makes sense. We will show later that the sensitivity of the solution to the value of cloud base q is relatively small above 5 km except for absolute temperature.

For M_c, we do not have a direct cloud base constraint. However, we assume our solution is in RCE, which says radiative cooling must be balanced by latent heat release at all levels. The RCE condition requires that M_c reaches 0 exactly at the level where the radiative cooling rate becomes 0, that is, at $T = 200$ K (Equation A13). If cloud base M_c is too large, M_c will still be positive where $T = 200$ K. If cloud base M_c is too small, M_c will go to 0 before radiative cooling decays to 0. We can have a random initial guess of cloud base M_c and change our guess based on this RCE condition. If this guess makes the M_c solution never go to 0 or go to 0 at higher and colder altitudes than $T = 200$ K, we need to reduce the guess. On the contrary, if the M_c solution goes to 0 at lower and warmer altitudes than $T = 200$ K, then we need to increase the guess. A solution is also not valid if the detrainment rate δ becomes negative during the upward integration. When this occurs, we examine the last level where δ remains positive. If $\delta > \epsilon$ at that level, it indicates that M_c is decaying too rapidly, resulting in a M_c value too small, causing the last term in Equation A25 to make δ turn negative. In this case, the initial guess for M_c is likely too small and should be increased. Conversely, if $\delta < \epsilon$ at that level, we choose to reduce our guess. Although this last criterion does not guarantee an upper bound, it works across a range of parameter regimes to find valid solutions in practice. Further investigation is warranted to establish a more robust criterion for the upper and lower bound. Once we find lower and upper bounds of the cloud base M_c, we use binary search to iteratively guess between the bounds and narrow the bounds until we find the M_c that satisfies the RCE condition.

In the case where $\mu = 0$ (i.e., no condensate evaporation and $s_{evap} = 0$ given Equation A8), Equation A25 becomes singular. We need to solve the equations in a slightly different way. By subtracting Equation A14 multiplied by L_v from Equation A16 and then using Equation A24, we can express M_c as a function of p, q, and T:

$$M_c(p, q, T) = -Q_{rad} \Big/ \frac{\partial s}{\partial z} \tag{A28}$$

where $s = c_p T + gz$ is the dry static energy in the environment, and $\partial s/\partial z = -c_p \Gamma + g$ is known from Equation A22. This expression for M_c automatically guarantees the RCE condition at the top boundary (M_c reaches 0 at the same level where radiative cooling becomes 0).

Using Equation A18, we can get an expression for δ:

$$\delta = \epsilon - \frac{1}{M_c} \frac{\partial M_c}{\partial z} \tag{A29}$$

Now with Equations A9, A19, and A22, we have come up with a slightly different ODE problem:

$$\frac{\partial}{\partial z}(p, q, T) = G(p, q, T, \delta) \tag{A30}$$

where the δ on the right-hand side depends on the LHS through Equations A28 and A29. This ODE problem should in principle be solvable using an implicit method, although we will leave this to future work.

In Figure A1 we test the sensitivity of the atmospheric profiles to the cloud base specific humidity (or equivalently RH). We change the cloud base RH from 70% to 90%. Except temperature profile, the influence of cloud base RH on other variables is primarily within the lower 5 km and does not have a big impact on the upper troposphere. The temperature becomes warmer through the whole troposphere with a moister cloud base environment. For cloud base mass flux, it strongly depends on the RH based on Equation 5 in the main text. The way we determine the cloud base RH using Equation A27 will implicitly lead to the sensitivity that cloud base mass flux increases when ϵ or μ increases. Since our main focus in this paper is the upper troposphere mass flux, the uncertainty in how we determine the cloud base RH will likely not change our results. We also tested fixing the relative humidity at the cloud base. The sensitivities regarding mixing strength and evaporation rate remain qualitatively the same. In future research, it would be beneficial to integrate considerations of energy and water conservation in the sub-cloud layer, along with surface flux parameterization, to automatically determine the cloud base relative humidity.

In Figure A2 we test the sensitivity to different sea surface temperatures. We can see that the whole troposphere becomes higher with the profiles of most quantities shifting upwards. The peak value of mass flux near the anvil
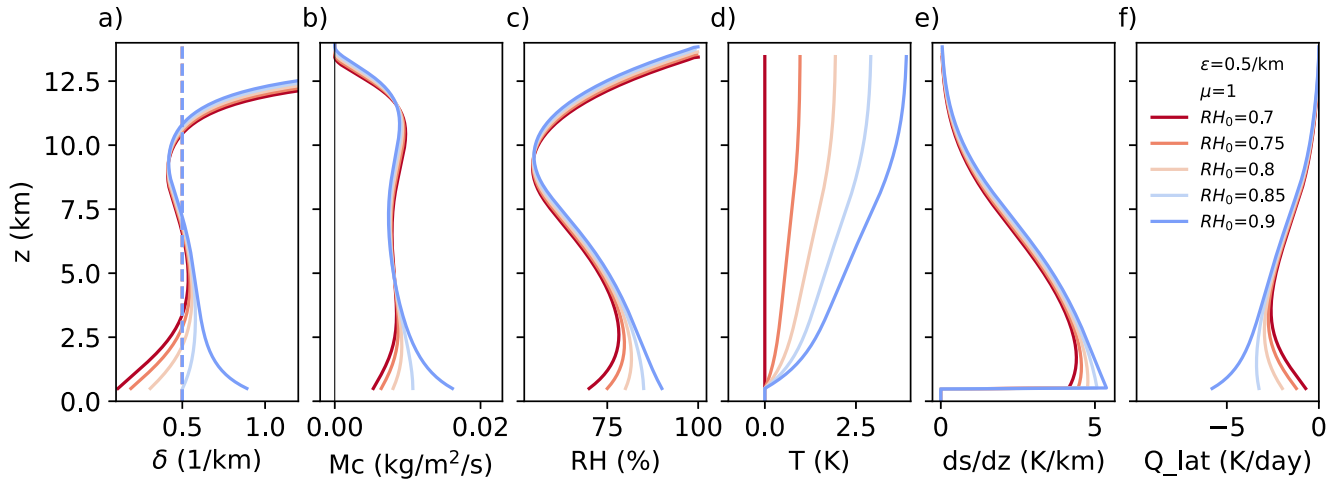
Figure A1. Atmosphere profiles in the zero-buoyancy plume model with varying cloud-base relative humidity (blue color represents more moist environment), entrainment rate $\epsilon = 0.5$ km^{-1}, and cloud evaporation parameter $\mu = 1$. The variables shown are (a) detrainment rate, (b) updraft mass flux, (c) relative humidity, (d) temperature, (e) the vertical gradient of dry static energy, and (f) latent heating rate due to cloud evaporation in the environment. Dashed lines in panel (a) are the profiles of the prescribed entrainment rate. The temperature in panel (d) is shown as deviation to one of the simulations, which is denoted by the red line with zero deviation.

level decreases with warmer surface temperature, which will indicate a weaker mass detrainment and likely a decrease of anvil cloud fraction (if the lifetime is assumed to be unchanged with surface warming). The decrease of upper troposphere mass flux is consistent with the stability iris effect proposed in Bony et al. (2016).

In Figure A3, we test the sensitivity of atmospheric profiles to varying ACRE. Since mass flux change could potentially change the anvil clouds and the associated cloud radiative heating, here we add cloud radiative heating term to explore the potential impact of cloud radiative heating on RCE solutions. The imposed ACRE is:

$$
\text{ACRE} = \begin{cases} 0.5H_0\left(1 + \cos\left(\pi\dfrac{T - 250}{30}\right)\right), & \text{if } 220K < T < 280K \\ 0, & \text{if } T < 220K \text{ or } T > 280K \end{cases}
$$

where H_0 is the peak ACRE value at $T = 250$ K. By increasing the ACRE together with increasing the entrainment rate, Figure A3b exhibits non-monotonic mass flux change. We may interpret this non-monotonic behavior from the energy balance view. On top of the effects of changing the mixing strength, at the heights where ACRE
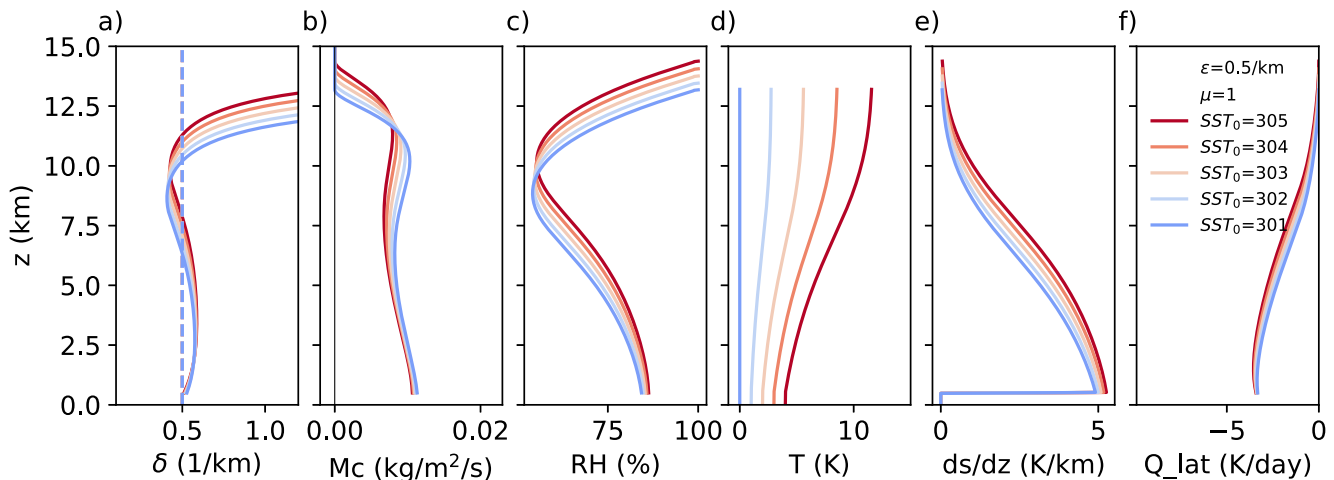

Figure A2. Similar to Figure A1 but with sea surface temperature (blue color represents colder surface temperature), entrainment rate $\epsilon = 0.5$ km^{-1}, and cloud evaporation parameter $\mu = 1$.
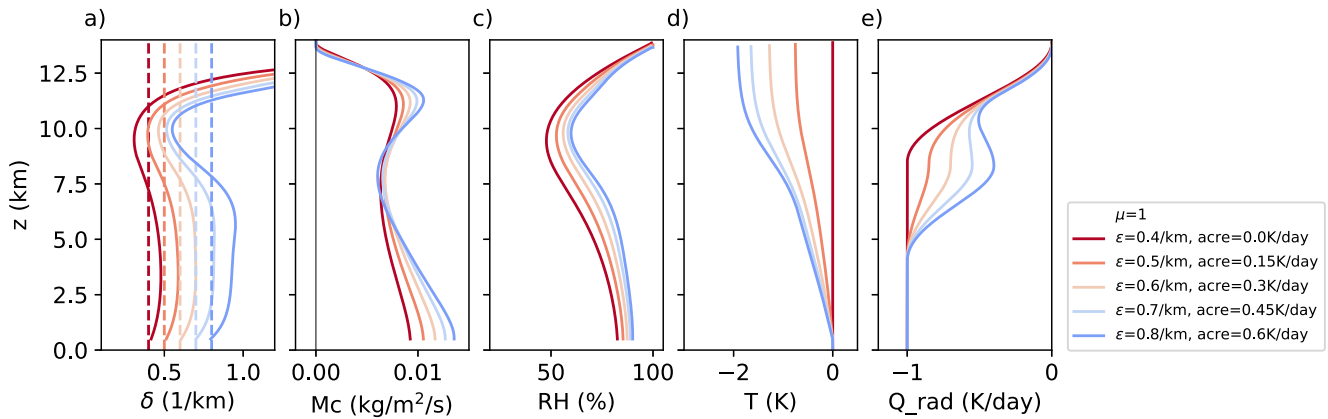
Figure A3. Similar to Figure 1 but with non-zero atmospheric cloud radiative effects (ACRE). Panel e shows the net radiative heating rate profiles. We use a fixed cloud evaporation parameter $\mu = 1$, increasing the entrainment rate ϵ from 0.4 to 0.8 km^{-1}, and increasing peak ACRE H_0 from 0 to 0.6 K/day.

increases, the net radiative cooling becomes weaker (Figure A3e), reducing the amount of mass flux needed to supply latent heating. Such interaction between the mixing strength and ACRE could partially explain the non-monotonic convective updraft mass flux change we observed in the numerical model simulations in Figure 5.

Appendix B: Relationship Between Cloud Evaporation and Perimeter Area Ratio

In the preceding sections, we highlighted the increased perimeter area ratio of cloud mass at higher resolutions, which potentially leads to greater exposure of the cloud mass to an unsaturated environment, thereby amplifying cloud evaporation. In this section, we derive a quantitative relationship between the cloud evaporation rate and the perimeter area ratio.

Consider a specific level with a unit thickness, where the cloud mass has a total area (A) and total perimeter (L). The clouds are advected in grid points through resolved horizontal wind with a representative speed of U_{adv}. Approximately half of the cloud boundary exhibits horizontal resolved wind pointing outwards from the cloud, while the other half features wind directed inward (Figure B1). After a time step dt, the volume of clouds advected across the boundary amounts to $0.5LU_{\text{adv}}dt$ (represented by the yellow area in Figure B1a). An equivalent volume of environmental air is advected into the original cloudy grids (illustrated by the orange area in Figure B1a). Following advection, the SAM1MOM scheme performs saturation adjustment. The yellow cloud mass becomes fully mixed with the environmental air in the respective grids, subsequently evaporating. On average, since the cloud mixing ratio near cloud edges is relatively minimal, we assume complete evaporation of the yellow cloud mass. The evaporation associated with this yellow cloud mass should be proportional to the product of the volume and the cloud mixing ratio at the edge $q_{\text{c,edge}}$. Similarly, in the grids containing orange environmental air, a portion of the cloud must evaporate to bring the unsaturated orange environmental air to saturation. The evaporation amount would be the product of the volume and the saturation deficit $q_{\text{v,env}}^*(1 - \mathcal{R})$, where $q_{\text{v,env}}^*$ represents the environmental saturation specific humidity and $\mathcal{R}$ is relative humidity. The total evaporation rate associated with saturation adjustment can be expressed as:

$$\textit{Evaporation} = 0.5LU_{\text{adv}}\rho\big[q_{\text{c,edge}} + q_{\text{v,env}}^*(1 - \mathcal{R})\big] \tag{B1}$$

We assume all this evaporation can be counted as in the environment. We further assume the total evaporation in the environment is dominated by this numerical diffusion associated with resolved horizontal wind. This assumption likely works well for high clouds where vertical wind and sub-grid diffusion are weak, but may not work well for low clouds where vertical wind and sub-grid diffusion could be strong. Total air mass in the environment can be written as $\rho A_d f_{\text{env}}$, where A_d is domain area, f_{env} is the fraction of environment. Therefore, the latent heating rate in the environment can be written as:
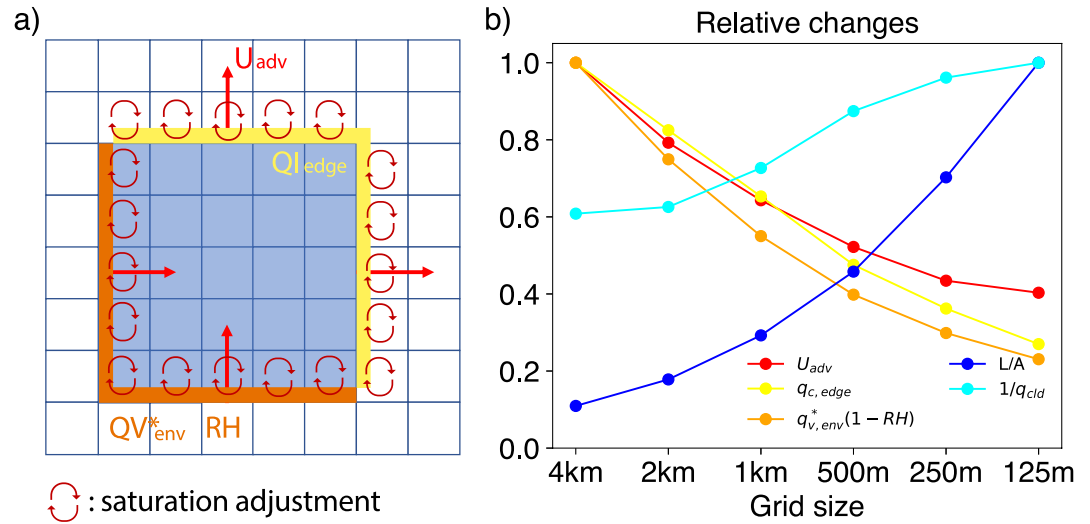
Figure B1. Panel (a) shows a schematic of cloud evaporation due to resolved horizontal advection and the following saturation adjustment in the SAM1MOM scheme. We set some clouds initially in the grids with blue shading and advect the cloud by the horizontal wind with $U_x = U_y = U_{adv}$. $q_{c,edge}$ is the cloud mixing ratio near the cloud edge. $q^*_{v,env}$ represents the environmental saturation specific humidity, and RH denotes relative humidity in the environment near the cloud. After a small timestep dt, some cloud mass is advected into environment grids (yellow shading), and some environmental mass is advected into cloudy grids (orange shading). Circular arrows represent the saturation adjustment in each grid due to the microphysics scheme. Panel (b) shows the relative value of different terms in Equation B4 in the SAM1MOM simulations with different resolutions. Each term is standardized (divided by the maximum value across the simulations with different resolutions) to have a value between 0 and 1.

$$Q_{lat,env} = 0.5LU_{adv}\left[q_{c,edge} + q^*_{v,env}(1-\mathcal{R})\right]\frac{L_v}{c_p A_d f_{env}} \tag{B2}$$

Since more clouds tend to generate more evaporation, we normalize the latent heating by the total cloud mass to get a quantity that reflects evaporation efficiency. Total cloud mass is proportional to the domain-mean cloud mixing ratio q_m, which can be further expressed as $q_m = f_{cld}q_{cld}$. f_{cld} is cloud fraction, and q_{cld} is the cloud mixing ratio averaged in cloudy grids. The normalized latent heating rate can be expressed as:

$$\frac{Q_{lat,env}}{q_m} = 0.5LU_{adv}\left[q_{c,edge} + q^*_{v,env}(1-\mathcal{R})\right]\frac{L_v}{c_p A_d f_{env} f_{cld} q_{cld}} \tag{B3}$$

Note that total cloud area can be written as $A = f_{cld}A_d$, the above equation can be rewritten as:

$$\frac{Q_{lat,env}}{q_m} = \frac{L}{A}U_{adv}\frac{q_{c,edge} + q^*_{v,env}(1-\mathcal{R})}{q_{cld}}\frac{L_v}{2c_p f_{env}} \tag{B4}$$

We define cloud boundaries as grid interfaces that separate a grid with zero cloud mixing ratio from a grid with non-zero cloud mixing ratio. Subsequently, we evaluate the average values of U_{adv}, $q_{c,edge}$, $q^*_{v,env}$, and $\mathcal{R}$ at grids immediately adjacent to the boundaries, either on the inside or the outside. In Figure B1b, we demonstrate the variation in different terms of Equation B4 as the resolution becomes finer. With increased resolution, the perimeter area ratio rises, while advection velocity, cloud mixing ratio, and environmental saturation deficit decrease. The decline in near-edge cloud mixing ratio and environmental saturation deficit could be attributed to the improved representation of the transition between cloudy grids and environmental grids at finer scales. The enhanced transition at cloud boundaries in higher resolutions tends to reduce numerical diffusion and partially counterbalance the effect of the growing perimeter area ratio. The cause of the weakened advection wind and reduced in-cloud mixing ratio remains unclear and merits further investigation.

Overall, finer resolution enables a better representation of turbulent cloud boundaries, enhancing the interaction between clouds and their environment. However, finer resolution also leads to a reduction in numerical diffusion. The interplay between these two effects may be crucial in determining whether cloud evaporation efficiency converges at a specific resolution. A comprehensive understanding of these factors is essential for improving the accuracy and reliability of Earth system models.

Data Availability Statement

The atmosphere model used to run the simulations is the System for Atmospheric Modeling (Khairoutdinov & Randall, 2003) and is available at http://rossby.msrc.sunysb.edu/~marat/SAM.html (version 6.10.6, Khairoutdinov, 2023). The figures in this manuscript, created by Python version 3.9, can be reproduced using the codes and data stored at https://doi.org/10.5281/zenodo.8397768 (Hu et al., 2024).

References

Bao, J.-W., Michelson, S., & Grell, E. (2019). Microphysical process comparison of three microphysics parameterization schemes in the WRF model for an idealized squall-line case study. *Monthly Weather Review*, *147*(9), 3093–3120. https://doi.org/10.1175/mwr-d-18-0249.1

Becker, T., Stevens, B., & Hohenegger, C. (2017). Imprint of the convective parameterization and sea-surface temperature on large-scale convective self-aggregation. *Journal of Advances in Modeling Earth Systems*, *9*(2), 1488–1505. https://doi.org/10.1002/2016ms000865

Beydoun, H., Caldwell, P. M., Hannah, W. M., & Donahue, A. S. (2021). Dissecting anvil cloud response to sea surface warming. *Geophysical Research Letters*, *48*(15), e2021GL094049. https://doi.org/10.1029/2021gl094049

Bony, S., Stevens, B., Coppin, D., Becker, T., Reed, K. A., Voigt, A., & Medeiros, B. (2016). Thermodynamic control of anvil cloud amount. *Proceedings of the National Academy of Sciences*, *113*(32), 8927–8932. https://doi.org/10.1073/pnas.1601472113

Bony, S., Stevens, B., Frierson, D. M., Jakob, C., Kageyama, M., Pincus, R., et al. (2015). Clouds, circulation and climate sensitivity. *Nature Geoscience*, *8*(4), 261–268. https://doi.org/10.1038/ngeo2398

Bretherton, C. S., McCaa, J. R., & Grenier, H. (2004). A new parameterization for shallow cumulus convection and its application to marine subtropical cloud-topped boundary layers. Part I: Description and 1D results. *Monthly Weather Review*, *132*(4), 864–882. https://doi.org/10.1175/1520-0493(2004)132<0864:anpfsc>2.0.co;2

Bryan, G. H., Wyngaard, J. C., & Fritsch, J. M. (2003). Resolution requirements for the simulation of deep moist convection. *Monthly Weather Review*, *131*(10), 2394–2416. https://doi.org/10.1175/1520-0493(2003)131<2394:rrftso>2.0.co;2

Hu, Z., Jeevanjee, N., & Kuang, Z. (2024). A refined zero-buoyancy plume model for large-scale atmospheric profiles and anvil clouds in radiative-convective equilibrium [Software]. *Zenodo*. https://doi.org/10.5281/zenodo.8397768

Hu, Z., Lamraoui, F., & Kuang, Z. (2021). Influence of upper-troposphere stratification and cloud–radiation interaction on convective overshoots in the tropical tropopause layer. *Journal of the Atmospheric Sciences*, *78*(8), 2493–2509. https://doi.org/10.1175/jas-d-20-0241.1

Iacono, M. J., Delamere, J. S., Mlawer, E. J., Shephard, M. W., Clough, S. A., & Collins, W. D. (2008). Radiative forcing by long-lived greenhouse gases: Calculations with the AER radiative transfer models. *Journal of Geophysical Research*, *113*(D13), D13103. https://doi.org/10.1029/2008jd009944

Igel, A. L., Igel, M. R., & van den Heever, S. C. (2015). Make it a double? Sobering results from simulations using single-moment microphysics schemes. *Journal of the Atmospheric Sciences*, *72*(2), 910–925. https://doi.org/10.1175/jas-d-14-0107.1

Jeevanjee, N. (2022). Three rules for the decrease of tropical convection with global warming. *Journal of Advances in Modeling Earth Systems*, *14*(11), e2022MS003285. https://doi.org/10.1029/2022ms003285

Jeevanjee, N., & Zhou, L. (2022). On the resolution-dependence of anvil cloud fraction and precipitation efficiency in radiative-convective equilibrium. *Journal of Advances in Modeling Earth Systems*, *14*(3), e2021MS002759. https://doi.org/10.1029/2021ms002759

Jenney, A., Ferretti, S., & Pritchard, M. (2023). Vertical resolution impacts explicit simulation of deep convection. *Journal of Advances in Modeling Earth Systems*, *15*(10), e2022MS003444. https://doi.org/10.1029/2022ms003444

Khairoutdinov, M. (2023). System for atmospheric modeling [Software]. *Stony Brook University*. Retrieved from http://rossby.msrc.sunysb.edu/~marat/SAM/

Khairoutdinov, M., & Randall, D. A. (2003). Cloud resolving modeling of the ARM summer 1997 IOP: Model formulation, results, uncertainties, and sensitivities. *Journal of the Atmospheric Sciences*, *60*(4), 607–625. https://doi.org/10.1175/1520-0469(2003)060<0607:crmota>2.0.co;2

Kuang, Z., & Bretherton, C. S. (2006). A mass-flux scheme view of a high-resolution simulation of a transition from shallow to deep cumulus convection. *Journal of the Atmospheric Sciences*, *63*(7), 1895–1909. https://doi.org/10.1175/jas3723.1

Lawson, R. P., & Cooper, W. A. (1990). Performance of some airborne thermometers in clouds. *Journal of Atmospheric and Oceanic Technology*, *7*(3), 480–494. https://doi.org/10.1175/1520-0426(1990)007<0480:posati>2.0.co;2

Morrison, H., Curry, J., & Khvorostyanov, V. (2005). A new double-moment microphysics parameterization for application in cloud and climate models. Part I: Description. *Journal of the Atmospheric Sciences*, *62*(6), 1665–1677. https://doi.org/10.1175/jas3446.1

Ohno, T., & Satoh, M. (2018). Roles of cloud microphysics on cloud responses to sea surface temperatures in radiative-convective equilibrium experiments using a high-resolution global nonhydrostatic model. *Journal of Advances in Modeling Earth Systems*, *10*(8), 1970–1989. https://doi.org/10.1029/2018ms001386

Ohno, T., Satoh, M., & Noda, A. (2019). Fine vertical resolution radiative-convective equilibrium experiments: Roles of turbulent mixing on the high-cloud response to sea surface temperatures. *Journal of Advances in Modeling Earth Systems*, *11*(6), 1637–1654. https://doi.org/10.1029/2019ms001704

Powell, S. W., Houze, R. A., Kumar, A., & McFarlane, S. A. (2012). Comparison of simulated and observed continental tropical anvil clouds and their radiative heating profiles. *Journal of the Atmospheric Sciences*, *69*(9), 2662–2681. https://doi.org/10.1175/jas-d-11-0251.1

Romps, D. M. (2014). An analytical model for tropical relative humidity. *Journal of Climate*, *27*(19), 7432–7449. https://doi.org/10.1175/jcli-d-14-00255.1

Romps, D. M. (2021). Ascending columns, WTG, and convective aggregation. *Journal of the Atmospheric Sciences*, *78*(2), 497–508. https://doi.org/10.1175/jas-d-20-0041.1

Romps, D. M., & Charn, A. B. (2015). Sticky thermals: Evidence for a dominant balance between buoyancy and drag in cloud updrafts. *Journal of the Atmospheric Sciences*, *72*(8), 2890–2901. https://doi.org/10.1175/jas-d-15-0042.1

Satoh, M., Stevens, B., Judt, F., Khairoutdinov, M., Lin, S.-J., Putman, W. M., & Düben, P. (2019). Global cloud-resolving models. *Current Climate Change Reports*, *5*(3), 172–184. https://doi.org/10.1007/s40641-019-00131-0

Seeley, J. T., Jeevanjee, N., Langhans, W., & Romps, D. M. (2019). Formation of tropical anvil clouds by slow evaporation. *Geophysical Research Letters*, *46*(1), 492–501. https://doi.org/10.1029/2018gl080747

Sherwood, S. C., Bony, S., & Dufresne, J.-L. (2014). Spread in model climate sensitivity traced to atmospheric convective mixing. *Nature*, *505*(7481), 37–42. https://doi.org/10.1038/nature12829

Siebesma, A., & Jonker, H. (2000). Anomalous scaling of cumulus cloud boundaries. *Physical Review Letters*, *85*(1), 214–217. https://doi.org/10.1103/physrevlett.85.214

Singh, M. S., & Neogi, S. (2022). On the interaction between moist convection and large-scale ascent in the tropics. *Journal of Climate*, *35*(14), 4417–4435. https://doi.org/10.1175/jcli-d-21-0717.1

Singh, M. S., & O'Gorman, P. A. (2013). Influence of entrainment on the thermal stratification in simulations of radiative-convective equilibrium. *Geophysical Research Letters*, *40*(16), 4398–4403. https://doi.org/10.1002/grl.50796

Singh, M. S., Warren, R. A., & Jakob, C. (2019). A steady-state model for the relationship between humidity, instability, and precipitation in the tropics. *Journal of Advances in Modeling Earth Systems*, *11*(12), 3973–3994. https://doi.org/10.1029/2019ms001686

Stevens, B., Satoh, M., Auger, L., Biercamp, J., Bretherton, C. S., Chen, X., et al. (2019). DYAMOND: The DYnamics of the Atmospheric general circulation Modeled On Non-hydrostatic Domains. *Progress in Earth and Planetary Science*, *6*(1), 1–17. https://doi.org/10.1186/s40645-019-0304-z

Zelinka, M. D., Myers, T. A., McCoy, D. T., Po-Chedley, S., Caldwell, P. M., Ceppi, P., et al. (2020). Causes of higher climate sensitivity in CMIP6 models. *Geophysical Research Letters*, *47*(1), e2019GL085782. https://doi.org/10.1029/2019gl085782

Zhou, W., & Xie, S. P. (2019). A conceptual spectral plume model for understanding tropical temperature profile and convective updraft velocities. *Journal of the Atmospheric Sciences*, *76*(9), 2801–2814. https://doi.org/10.1175/JAS-D-18-0330.1